

Extending the Radial Acceleration Relation using Weak Gravitational Lensing with the Kilo-Degree Survey

Margot M. Brouwer^{1,2*}, Kyle A. Oman^{1,3}, Edwin A. Valentijn¹, et al.

¹*Kapteyn Astronomical Institute, University of Groningen, PO Box 800, NL-9700 AV Groningen, the Netherlands.*

²*Institute for Theoretical Physics, University of Amsterdam, Science Park 904, 1098 XH Amsterdam, The Netherlands.*

³*Institute for Computational Cosmology, Department of Physics, Durham University, South Road, Durham DH1 3LE, UK*

Accepted XXX. Received YYY; in original form ZZZ

ABSTRACT

To be written.

Key words: gravitational lensing: weak – Surveys – methods: statistical – galaxies: haloes – cosmology: dark matter, theory – gravitation.

* E-mail: brouwer@astro.rug.nl

1 INTRODUCTION

It has been known for several decades that the outer regions of galaxies rotate faster than would be expected from Newtonian dynamics based on their luminous, or ‘baryonic’, mass. This was first discovered by Rubin (1983) through measuring galactic rotation curves of optical disks, and by Bosma (1981) through measuring hydrogen profiles at radii beyond the disk. The excess gravity implied by these measurements has been generally attributed to an unknown and invisible substance named Dark Matter (DM), a term coined more than forty years prior by Zwicky (1937) when he discovered the so-called ‘missing mass problem’ through the dynamics of galaxies in clusters.

Following more recent observations using Weak gravitational Lensing (WL, Hoekstra et al. 2004; von der Linden et al. 2014; Mandelbaum 2015), Baryon Acoustic Oscillations (BAO’s, Eisenstein et al. 2005; Blake et al. 2011) and the Cosmic Microwave background (CMB, Spergel et al. 2003; Planck XVI 2014), Cold Dark Matter¹ (CDM) became a key ingredient of the current standard model of cosmology: the Λ CDM model. In this paradigm, CDM accounts for $\Omega_{\text{CDM}} = 0.266$ of the critical density in the Universe, while baryonic matter only accounts for $\Omega_{\text{CDM}} = 0.049$ (Planck VI 2018). The cosmological constant Λ , which is necessary to explain the accelerated expansion of the Universe and is usually associated with Dark Energy (DE), accounts for $\Omega_{\Lambda} = 0.685$.

Although the Λ CDM model successfully describes the behaviour of DM on a wide range of scales, no conclusive evidence for the existence of DM particles has been found so far (despite years of enormous effort; for an overview, see Bertone et al. 2005; Bertone & Tait 2018). This still leaves some room for alternative theories of gravity, such as Modified Newtonian Dynamics (MOND, Milgrom 1983) and the more recent theory of Emergent Gravity (EG, Verlinde 2016). In these theories particle DM does not exist, and all gravity is due to the baryonic matter (or, in the case of EG, the interaction between baryons and the entropy associated with DE). Hence, one of the main properties of these theories is that the mass discrepancy in galaxies correlates strongly with their baryonic mass distribution.

Such a correlation has indeed been widely observed. First, astronomers discovered the Tully-Fisher relation (TFR, Tully & Fisher 1977) between the luminosity of a spiral galaxy and its asymptotic rotation velocity (Pierce & Tully 1988; Bernstein et al. 1994). Since this corresponds to a relation between the baryonic and the total galaxy mass, this has later been named the ‘baryonic’ TFR (BTFR, McGaugh et al. 2000; McGaugh 2012). As the radial resolution of observations increased, astronomers found a strong correlation between the observed rotation velocity $v_{\text{obs}}(r)$ as a function of galaxy radius r , and the enclosed luminous mass $M_b(< r)$ (Sanders 1986, 1996; McGaugh 2004; Sanders & Noordermeer 2007; Wu & Kroupa 2015). Since $M_b(< r)$ corresponds to the *expected* gravitational acceleration $g_b(r)$ from baryonic matter, and the observed gravitational acceleration can be calculated through $g_{\text{obs}}(r) = v_{\text{obs}}^2(r)/r$, this

relation has been named the Radial Acceleration Relation (RAR)².

Particularly, the latest results from McGaugh et al. (2016) (hereafter M16) have measured the RAR relation with unprecedented accuracy, using the Spitzer Photometry and Accurate Rotation Curves (SPARC, Lelli et al. 2016) data of 153 late-type galaxies. Their results showed a tight correlation between g_{obs} and g_{bar} , which they could fit using a simple double power law (Eq. 4 in M16) depending only on g_{bar} and one free parameter: the acceleration scale g_{\dagger} where Newtonian gravity appears to break down. This sparked the interest of scientists working on alternative theories of gravity, but also of those in favor of a statistical explanation of the RAR within the Λ CDM framework (Keller & Wadsley 2017; Desmond 2017; Ludlow et al. 2017).

The latter possibility was quantified by Navarro et al. (2017) (hereafter N17) who used a range of simplifying assumptions based on galaxy observations and DM simulations, in order to create an analytical galaxy+halo model. The goal of their model was to reconstruct the RAR in galaxies, in particular the value of a_0 : the acceleration scale where the relation transitions from the baryon-dominated to the DM-dominated regime (which is equivalent to g_{\dagger}), and a_{min} : the minimum acceleration probed by galaxy disks. Based on their results, they claimed that the RAR can be explained within the Λ CDM framework, at the accelerations probed by galaxy rotation curves (i.e. $g_{\text{obs}} > a_{\text{min}}$). However, since their model relies on the fact that luminous kinematic tracers in galaxies only probe a limited radial range, N17 predicted that extending observations to radii beyond the disk (which correspond to lower gravitational accelerations) would lead to systematic deviations from the simple relation posed by M16.

The goal of this work is to extend observations of the RAR to lower accelerations, which are not measurable using galaxy rotation curves. To this end we use gravitational lensing: the perturbation of light inside a gravitational potential as described by General Relativity (GR). In particular, we use the method of Galaxy-Galaxy Lensing (GGL): the statistical measurement of the coherent image distortion (shear) of a field of background galaxies by the gravitational potential of a sample of foreground galaxies (for examples, see e.g. Fischer et al. 2000; Hoekstra et al. 2004; Mandelbaum et al. 2006; van Uitert et al. 2016). Using GGL we can measure the average (apparent) density distribution of galaxies up to a radius of 3 Mpc, roughly a 100 times larger than the radius of the luminous disk (~ 30 kpc), corresponding to a value of g_{bar} that is 3 orders of magnitude lower than those measurable with galaxy rotation curves.

First, we measure the baryonic and total density profiles of our galaxies through their luminosities and GGL profiles. These measurements will be performed using photometric data from Sloan Digital Sky Survey (Abazajian et al. 2009, SDSS,) and the VISTA Kilo-Degree Infrared Galaxy survey (Edge et al. 2013, VIKING), and WL data from the Kilo-

¹ DM particles that moved at non-relativistic speeds at the time of recombination, as favoured by measurements of the CMB (Planck XVI 2014) and the Lyman- α forest (Viel et al. 2013).

² Another well-established name for this same relation is the Mass-Discrepancy Acceleration Relation (MDAR), which refers to the correspondence between the observed baryonic/total mass and the inferred mass discrepancy commonly attributed to DM. Throughout this work we use the term RAR for brevity.

Degree Survey (KiDS; de Jong et al. 2013). We then translate these measurements into the baryonic and observed radial accelerations, g_{bar} and g_{obs} . Finally, we compare the resulting RAR to predictions from different modified gravity theories (MOND and EG) and Λ CDM.

The Λ CDM predictions will not only be provided by the N17 analytical model, but also by two mock galaxy catalogues based on two different DM simulations. One is the Marenostrum Institut de Ciències de l’Espai (MICE) Galaxy and Halo Light-cone catalogue (Carretero et al. 2015; Hoffmann et al. 2015), which is based on the MICE Grand Challenge lightcone simulation (MICE-GC, Fosalba et al. 2015a,b; Crocce et al. 2015). The other mock galaxy catalogue is based on a suite of large-volume cosmological hydrodynamical simulations, which is called the Baryons and HALoes of MAssive Systems (BAHAMAS) project (McCarthy et al. 2017). Our first goal is to distinguish which of the aforementioned predictions best describe the RAR at lower accelerations.

Having almost a million foreground galaxies at our disposal, we are able to select specific galaxy samples designed to optimally test these predictions. Particularly, we note that most models (MOND, EG, and the N17 analytical DM model) focus on the description of individual, isolated galaxies. In order to test them, therefore, we select a sample of galaxies whose lensing profiles are not affected by their neighbours within the radius of our measurement. In contrast, the predictions from the MICE and BAHAMAS simulations can be tested for both isolated and non-isolated galaxy samples.

Furthermore, we note that all models give a specific prediction regarding the dependence of the RAR on baryonic galaxy mass. According to the MOND and EG theories, the relation between g_{bar} and g_{obs} should remain intact in the regime beyond the disk, independent of the disk mass. Within the Λ CDM paradigm, however, all predictions (analytical and simulated) are based on a ‘stellar-to-halo-mass relation’ which is not constant as a function of baryonic galaxy mass. By splitting our foreground galaxies into bins of increasing stellar mass, we are able to better distinguish the predictions of these different models.

Our paper is structured as follows. In Sect. 2 we introduce our main datasets: both the KiDS and GAMA galaxy surveys which are used to perform the GGL measurements, and the MICE and BAHAMAS simulations & mock galaxy catalogues to which we compare our results. Sect. 3 describes our analysis of these (mock) datasets as we select our isolated foreground galaxy sample, perform the GGL measurements, and translate the results into the RAR. Sect. 5 contains a description of the theoretical predictions to which we compare our observations: MOND, EG and the N17 analytical DM model. In Sect. 6 we present the resulting RAR measurements and model comparison. Sect. 7 contains the discussion and conclusion.

Throughout this work we adopt the WMAP 9-year (Hinshaw et al. 2013) cosmological parameters: $\Omega_m = 0.2793$, $\Omega_b = 0.0463$, $\Omega_\Lambda = 0.7207$, $\sigma_8 = 0.821$ and $H_0 = 70 \text{ km s}^{-1} \text{ Mpc}^{-1}$, which were used as the basis of the BAHAMAS simulation. The cosmological parameters used in creating the MICE-GC simulations are: $\Omega_m = 0.25$, $\sigma_8 = 0.8$, $\Omega_\Lambda = 0.75$, and $H_0 = 70 \text{ km s}^{-1} \text{ Mpc}^{-1}$. Through-

out the paper we use the reduced Hubble constant $h_{70} \equiv H_0 / (70 \text{ km s}^{-1} \text{ Mpc}^{-1})$.

2 DATA

2.1 KiDS source galaxies

We use Galaxy-Galaxy Lensing (GGL) to measure the gravitational potential around a sample of foreground galaxies (lenses), by measuring the image distortion (shear) of a field of background galaxies (sources). These sources are observed using OmegaCAM (Kuijken 2011): a 268-million pixel CCD mosaic camera mounted on the VLT Survey Telescope (Cappacioli & Schipani 2011). Over the past seven years these instruments have performed KiDS, a photometric survey in the *ugri* bands, which is especially designed to perform WL measurements (de Jong et al. 2013).

GGL studies with KiDS have hitherto been performed in combination with the spectroscopic GAMA survey (see Sect. 2.2 below). Already since the previous data release (KiDS-DR3, de Jong et al. 2017) the KiDS survey completely covers the 286 deg^2 GAMA area. Although the final survey will span 1350 deg^2 on the sky, the current state-of-the-art is the 4th Data Release (KiDS-DR4, Kuijken et al. 2019) containing observations from 1006 square-degree survey tiles. The measurement of the source shapes and photometric redshifts are performed in similar fashion to de Jong et al. (2017). Changes and improvements to these methods are described in Kuijken et al. (2019).

The measurements of the galaxy shapes are based on the *r*-band data, since this filter was used during the darkest time (moon distance $> 90 \text{ deg}$) and with the best atmospheric seeing conditions ($< 0.8 \text{ arcsec}$). The *r*-band observations are co-added using the THELI pipeline (Erben et al. 2013), which is improved through the addition of an illumination correction. From these images the galaxy positions are detected through the SExtractor algorithm (Bertin & Arnouts 1996). After detection, the shapes of the galaxies are measured using the *lensfit* pipeline (Miller et al. 2007, 2013), which includes a self-calibration algorithm based on Fenech Conti et al. (2017). Each shape is accompanied by a *lensfit* weight w_s , which gives an estimate of the precision of the ellipticity measurement.

For the purpose of creating the photometric redshift and stellar mass estimates, eight additional bands are observed. The *u*, *g* and *i* bands are observed by KiDS, while the VISTA Kilo-degree Infrared Galaxy survey (VIKING, Edge et al. 2013) performed on the VISTA telescope adds the *ZYJHK_s* bands. All bands are reduced and co-added using the Astrowise (AW) pipeline (McFarland et al. 2013). The galaxy colours, which form the basis of the photometric redshift measurements, are measured from these images using the Gaussian Aperture and PSF pipeline (GAAP Kuijken 2008; Kuijken et al. 2015).

The addition of the lower frequency VISTA data allows us to extend the redshift estimates out to $0.1 < z_B < 1.2$ (instead of $0.1 < z_B < 0.9$ in KiDS-DR3), where z_B is the best-fit photometric redshift of the sources (Benítez 2000; Hildebrandt et al. 2012). However, when performing our lensing measurements (see 3.1) we use the total redshift probability distribution function (PDF) n_z of the full source population.

This n_z is calculated using the direct calibration method (DIR, [Hildebrandt et al. 2017](#)), and circumvents the inherent bias related to photometric redshift estimates of individual sources.

2.2 GAMA foreground galaxies

Although the final RAR measurements will be performed using exclusively the KiDS-DR4 data, the set of foreground galaxies observed by the spectroscopic GAMA survey ([Driver et al. 2011](#)) function both as a model and validation sample for the KiDS foreground galaxies. The survey was performed by the Anglo-Australian Telescope with the AAOmega spectrograph, and targeted more than 180 000 galaxies that were selected from SDSS. For this study we use the GAMA II data release ([Liske et al. 2015](#)) consisting of three equatorial regions (G09, G12 and G15). These regions span a total area of $\sim 180 \text{ deg}^2$ on the sky, completely overlapping with KiDS.


GAMA has a redshift range of $0 < z < 0.5$, with a mean redshift of $\langle z \rangle = 0.22$. The survey has a redshift completeness of 98.5% down to Petrosian r -band magnitude $m_{r,\text{Petro}} = 19.8 \text{ mag}$. We limit our GAMA foreground sample to galaxies with the recommended redshift quality: $n_Q \geq 3$. The GAMA spectroscopic redshifts are used to train the photometric machine-learning (ML) redshifts of our larger sample of KiDS foreground galaxies (see Sect. 2.3).

Despite being a smaller survey, GAMA's accurate redshifts are highly advantageous when measuring the ESD profiles of galaxies (see Sect. 3.1). Also, in combination with its high redshift completeness, GAMA allows for a better application of the isolation criterion. We therefore check that the results from the KiDS-only measurements are consistent with those from KiDS-GAMA at all times.

To measure the RAR with KiDS-GAMA, we need individual stellar masses M_* for each GAMA galaxy. These are measured from their *ugrizZYJHK* Spectral Energy Distributions (SEDs)³ measured by SDSS and the VISTA Kilo-Degree Infrared Galaxy survey (VIKING, [Edge et al. 2013](#)), by fitting them with [Bruzual & Charlot \(2003\)](#) Stellar Population Synthesis (SPS) models, using the Initial Mass Function (IMF) of [Chabrier \(2003\)](#). Following the procedure described by [Taylor et al. \(2011\)](#), we account for flux falling outside the automatically selected aperture using the 'flux-scale' correction.

2.3 KiDS foreground selection

As our lenses, we select a 'GAMA-like' (GL) sample of foreground galaxies from $\sim 1000 \text{ deg}^2$ of KiDS-DR4 data ([Kuijken et al. 2019](#)). To mimic the magnitude limit of GAMA ($m_{r,\text{Petro}} < 19.8 \text{ mag}$), we apply a similar cut to the (much deeper) KiDS survey. Because the KiDS catalogue does not contain Petrosian magnitudes, we use the calibrated Kron-like elliptical aperture r -band magnitudes 'MAG_AUTO_CALIB' from SExtractor, which have a very similar distribution. Through matching the KiDS and

GAMA galaxies and seeking the best trade-off between completeness and purity, we decide to limit our GL-KIDS sample to $m_{r,\text{auto}} < 20.0$. In addition, we limit the redshifts of the GL-KiDS galaxies to the maximum GAMA redshift ($z_G < 0.5$). 

To remove any stellar contamination we apply three independent cuts: based on galaxy morphology, the 9-band photometry, and the SExtractor star/galaxy classifier respectively⁴. We also remove galaxies that are affected by readout and diffraction spikes, saturation cores, bad pixels, or by primary, secondary or tertiary haloes of bright stars⁵. In addition, we apply the recommended '9-band no AW- r -band mask', which is also used to create the KiDS-DR4 shear catalogues⁶. Our final sample GL-KiDS lenses consists of 9.85×10^5 galaxies with a mean redshift of $\langle z_{\text{ANN}} \rangle = 0.24$, which slightly higher than that of GAMA ($\langle z \rangle = 0.22$). As mentioned, we apply the GAMA redshift limit to the GL-KiDS galaxies ($z_{\text{ANN}} < 0.5$), after which the two mean redshifts are equal.

To apply the aforementioned redshift limit, and more importantly to use the GL-KiDS sample as lenses to measure g_{obs} , we need accurate individual redshifts for all galaxies in our sample. These photometric redshifts z_{ANN} are derived from the full 9-band KiDS+VIKING photometry (see Sect. 2.1), by training on the spectroscopic GAMA redshifts (see Sect. 2.2) using the ANNz2 machine learning method ([Sadeh et al. 2016](#); [de Jong et al. 2017](#); [Bilicki et al. 2017](#)). Objects that are not detected in all 9 bands are removed from the sample. When comparing the z_{ANN} to the spectroscopic z_G redshifts measured for the same galaxies, we find that their mean fractional offset is $\langle (z_{\text{ANN}} - z_G)/z_G \rangle = 0.036$. However, this offset is mainly caused by the low-redshift galaxies: $z_{\text{ANN}} < 0.1$. Removing these decreases the mean offset to $\langle \delta z/z_G \rangle = 0.0063$, with a standard deviation $\sigma_z = 0.026$. This corresponds to a redshift-dependent deviation of $\sigma_z/(1 + \langle z_{\text{ANN}} \rangle) = 0.021$ based on the mean redshift of GL-KiDS between $0.1 < z_{\text{ANN}} < 0.5$ ($\langle z_{\text{ANN}} \rangle = 0.24$), which is the lens redshift range we use throughout this work for all lens samples.

In order to measure the expected baryonic acceleration g_{bar} , we compute stellar masses $M_{*,\text{ANN}}$ based on these ANNz2 redshifts and the 9-band GAAP photometry. This is achieved using the LePHARE algorithm ([Arnouts et al. 1999](#); [Ilbert et al. 2006](#)) to perform SPS model fits on the stellar component of the galaxy SED. The used SPS model is [Bruzual & Charlot \(2003\)](#), with the IMF from [Chabrier \(2003\)](#) (equal to those used for the GAMA stellar masses). LePhare provides both the best-fit M_* value 'MASS_BEST' of the galaxy template PDF, and the 68% confidence level upper and lower limits. Because the GAAP photometry only measures the galaxy magnitude within a specific aperture size, this stellar mass is corrected using a 'fluxscale' pa-

³ The SEDs are constrained to the rest frame wavelength range 3000 – 110000 Å.

⁴ Our star-galaxy separation corresponds to applying the following flags: SG2DPHOT=0, SG_FLAG=1, CLASS_STAR<0.5.

⁵ This masking corresponds to applying all MASK values (1, 2, 4, 8, 16, 32 and 64) described in App. A.1.1 of [Kuijken et al. \(2019\)](#), through applying the flag: IMAFLAGS_ISO=0.

⁶ This masking corresponds to the 9-band MASK bit values 2 to 11, 13 and 14, described in App. A.2 of [Kuijken et al. \(2019\)](#). For more information on these masks, we refer the reader to App. A of [Kuijken et al. \(2019\)](#).

parameter, such that: $M_* = \text{M_BEST} + (\text{MAG_GAAP_r} - \text{MAG_AUTO_CALIB}) / 2.5$.

When comparing $M_{*,\text{ANN}}$ with the GAMA stellar masses $M_{*,\text{G}}$ of matched galaxies we find that its distribution is very similar, with a standard deviation of 0.21 dex. Nevertheless there exists a systematic offset of $\log(M_{*,\text{ANN}}) - \log(M_{*,\text{G}}) = -0.056$ dex, which is caused by the different stellar mass estimation methods used on the two surveys. In general, it has been found impossible to constrain stellar masses within a systematic uncertainty of $\Delta M_* \sim 0.2$ dex when applying different methods, even when the same SPS, IMF and data are used (Taylor et al. 2011; Wright et al. 2017). We therefore normalize the $M_{*,\text{ANN}}$ values of our GL-KiDS sample to the mean $M_{*,\text{G}}$ of GAMA, while indicating throughout our results the range of possible bias due to a $\Delta M_* = 0.2$ dex systematic shift in M_* . We estimate the effect of this bias by computing the RAR with $\log(M_*) \pm \Delta M_*$ as upper/lower limits.

2.4 MICE mock galaxies

In order to compare our observations to Λ CDM-based predictions, we use two different sets of simulations. One of these is the MICE-GC N -body simulation, which contains $\sim 7 \times 10^{10}$ DM particles in a $(3072 h_{70}^{-1} \text{Mpc})^3$ comoving volume (Fosalba et al. 2015b). From this simulation the MICE collaboration constructed a $\sim 5000 \text{ deg}^2$ lightcone with a maximum redshift of $z = 1.4$. The DM halos in this lightcone are identified using a Friend-of-Friend (FOF) algorithm on the particles. These DM halos were populated with galaxies using a hybrid Halo Occupation Distribution (HOD) and Halo Abundance Matching (HAM) prescription (Carretero et al. 2015; Crocce et al. 2015).

In the MICECATv2.0 catalogue⁷ which we use in this work, every galaxy has sky coordinates, redshifts, comoving distances, apparent magnitudes and absolute magnitudes assigned to them. We use the SDSS apparent r -band magnitudes m_r , as these most closely match those from KiDS (see Brouwer et al. 2018). We can therefore limit the MICE galaxies to the same apparent magnitude as the GL-KiDS sample: $m_r < 20$ mag, in order to create a GL-MICE foreground galaxy sample. We also use the same redshift limit: $0.1 < z < 0.5$, resulting in a mean GL-MICE redshift $\langle z \rangle = 0.23$, almost equal to that of GAMA and GL-KiDS within this range. The absolute magnitudes of the mock galaxies go down to $M_r - 5 \log_{10}(h) < -14$ mag, which corresponds to the faintest GAMA and GL-KiDS galaxies. New to this version, is that each galaxy is also assigned a stellar mass M_* needed to compute the RAR (see Sect. 4). These stellar masses are determined from the galaxy luminosities L using Bell & de Jong (2001) M/L ratios.

In addition, each galaxy has a pair of lensing shear values associated with it (γ_1 and γ_2 , with respect to the Cartesian coordinate system). These shear values were calculated from healpix weak lensing maps that were constructed using the ‘onion shell method’ (Fosalba et al. 2008, 2015a). The lensing map of MICECATv2.0 has an improved resolution of 0.43 arcmin, which is almost twice smaller than

that of MICECATv1.0 (0.85 arcmin). At the mean GL-MICE redshift this resolution corresponds to a projected distance of $R = 0.11 h^{-1} \text{Mpc}$. Throughout this work, we will not use MICE data that is within two times this radius: $R = 0.22 h^{-1} \text{Mpc}$.

At scales larger than this limit, the MICE shears allow us approximate the lensing analysis we perform on our KiDS data (as described in Section 3.1) using the MICE simulation. To create a sample of MICE background galaxies for the lensing analysis, we apply limits on the MICE mock galaxies’ redshifts and apparent magnitudes which are analogous to those applied to the KiDS source sample: $0.1 < z < 1.2$, $m_r > 20$ (see Hildebrandt et al. 2017 and Sect. 2.1; note that uncertainties in the KiDS z_B are not accounted for in this selection). We also apply an absolute magnitude cut of $M_r > -18.5$ mag, in order to resemble the KiDS source redshift distribution more closely.

The MICE-GC mock catalogue also features very accurate clustering. At lower redshifts ($z < 0.25$) the clustering of the mock galaxies as a function of luminosity is constructed to reproduce the SDSS clustering observations (Zehavi et al. 2011), while at higher redshifts ($0.45 < z < 1.1$) it was validated against the Cosmic Evolution Survey (COSMOS, Ilbert et al. 2009). This makes MICE especially suitable to reproduce the RAR at larger scales ($> 1 h^{-1} \text{Mpc}$) where neighbouring galaxies start to affect the lensing signal, and to test our criteria considering the galaxy isolation (see Section 3.2).

2.5 BAHAMAS mock galaxies

The second set of simulations which we utilize is the BAHAMAS⁸ suite of McCarthy et al. (2017). The BAHAMAS runs are smoothed-particle hydrodynamical realizations of $(400 h^{-1} \text{Mpc})^3$ volumes and include prescriptions for radiative cooling/heating, ionizing background radiation, star formation, stellar evolution & chemical enrichment, (kinetic wind) supernova feedback, and supermassive black hole accretion, merging & (thermal) AGN thermal feedback. The simulations are calibrated to reproduce the stellar and hot gas content of massive haloes, which makes them particularly well-suited for our study of the matter content of haloes at $\approx 1\text{--}3 \text{Mpc}$. The masses of dark matter and baryonic resolution elements are 3.85×10^9 and $7.66 \times 10^8 h^{-1} M_\odot$, respectively, and the gravitational softening is fixed at $4 h^{-1} \text{kpc}$. In addition to the calibrated fiducial model, we also make use of two model variations, ‘hi AGN’ and ‘low AGN’, where the AGN heating temperature is varied by ± 0.2 dex (McCarthy et al. 2018), and a ‘dark matter-only’ (DMO) volume where the baryons are modelled as collisionless and dissipationless, which in practice behave as additional dark matter. The volumes which we use assume the WMAP9 values for the cosmological parameters, which differs from the Planck values assumed throughout the rest of this work. Where relevant, we re-scale coordinates, masses, etc. to account for the difference in the Hubble constant.

Haloes and galaxies are identified in the simulations using the FOF (Davis et al. 1985) and Subfind (Springel et al.

⁷ The MICECATv2.0 catalogue is available through CosmoHub (<https://cosmohub.pic.es>).

⁸ Baryons and Haloes of MAssive Systems.

2001; Dolag et al. 2009) algorithms. We label the most massive subhalo in each FOF group as the ‘central’ and other subhaloes as ‘satellites’. We randomly select 100 central subhaloes at $z = 0.25$ from the DMO simulation in each of a series of 0.25 dex bins in $12 < \log_{10}(M_{500}/M_{\odot}) < 15$ (in the highest mass bin there are less than 100 haloes; we select them all). In order to construct a consistent sample, the same haloes are then identified in the fiducial and hi/low AGN volumes. We also construct an ‘isolated’ sample by restricting the selection to central subhaloes which have no subhaloes more massive than 10 per cent of their mass within 3 Mpc. For each selected galaxy, we construct an integrated surface density map at ~ 25 kpc resolution, integrated along the line of sight for ± 25 Mpc around the target halo. We also extract the cumulative spherically averaged mass profile of each target subhalo, decomposed into dark matter, stars and gas. For both the maps and profiles, we include mass contributions from all surrounding (sub)structures, i.e. we do not isolate the haloes from their surrounding environment.

3 DATA ANALYSIS

3.1 Lensing measurement

The measurement of the projected mass density that we use to estimate the gravitational acceleration around galaxies (see Sect. 4), is obtained through the WL method (for a general introduction, see Bartelmann & Schneider 2001; Schneider et al. 2006). More specifically, we use GGL: the measurement of the coherent image distortion of a field of background galaxies (sources) by the gravitational potential of a sample of foreground galaxies (lenses). Because the individual image distortions are very small (only $\sim 1\%$ compared to the galaxy’s unknown original shape), this method can only be performed statistically for a large sample of sources. We average their projected ellipticity component ϵ_t tangential to the direction of the lens galaxy, which is the sum of the intrinsic ellipticity ϵ_{int} and the tangential shear γ_t caused by WL. Assuming no preferential alignment in the intrinsic galaxy shapes ($\langle \epsilon_{\text{int}} \rangle = 0$), the average $\langle \epsilon_t \rangle$ is an estimator of γ_t . By measuring this averaged quantity in circular annuli around the lens centre, we obtain the shear profile $\gamma_t(R)$ as a function of projected radius R .

The lensing shear profile can be related to the physical Excess Surface Density (ESD) profile:

$$\Delta\Sigma(R) = \Sigma_{\text{crit}}\gamma_t(R) = \langle \Sigma \rangle(< R) - \Sigma(R), \quad (1)$$

which is the surface density $\Sigma(R)$ at projected radius R , subtracted from the average surface density $\langle \Sigma(< R) \rangle$ within R . The conversion factor between γ_t and $\Delta\Sigma$ is the critical surface density, whose inverse is also called the lensing efficiency:

$$\Sigma_{\text{crit}}^{-1} = \frac{4\pi G}{c^2} \int_0^\infty D(z_1) \left(\int_{z_1}^\infty \frac{D(z_1, z_s)}{D(z_s)} n(z_s) dz_s \right) p(z_1) dz_1, \quad (2)$$

where $D(z_1)$ and $D(z_s)$ are the angular diameter distances to the lens and the source respectively, and $D(z_1, z_s)$ the distance between them. The constant multiplication factor is defined by Newton’s gravitational constant G and the speed of light c . For the lens redshifts z_1 , we use the ANNz machine-learning redshifts of the KiDS

foreground galaxy sample (see Sect. 2.3). We implement the contribution of z_1 by integrating over the individual redshift probability distributions $p(z_1)$ of each lens. This $p(z_1)$ is defined by a normal distribution centred at the lens’ z_{ANN} redshift, with a standard deviation: $\sigma_z/(1+z) = 0.018$. For the source redshifts z_s we follow the method used in Dvornik et al. (2018), by integrating over the part of the redshift probability distribution $n(z_s)$ where $z_s > z_1$. In addition, sources only contribute their shear to the lensing signal when $z_B + \Delta z > z_1$, i.e. the sum of their best-fit photometric redshift z_B and the redshift buffer $\Delta z = 0.2$ is greater than the lens redshift. Following Brouwer et al. (2017), we measure the ESD profiles between: $0.03 < R < 30 h^{-1}\text{Mpc}$.

To increase the signal-to-noise ratio (S/N) of the lensing signal even further, the ESD profile is averaged (or ‘stacked’) for large samples of lenses. We define a lensing weight W_{ls} which depends on both the *lensfit* weight w_s and the lensing efficiency $\Sigma_{\text{crit}}^{-1}$:

$$W_{\text{ls}} = w_s \left(\Sigma_{\text{crit}, \text{ls}}^{-1} \right)^2, \quad (3)$$

and use it to optimally sum the measurements from all lens-source pairs into the average ESD:

$$\Delta\Sigma = \frac{1}{1+\mu} \frac{\sum_{\text{ls}} W_{\text{ls}} \epsilon_{t, \text{ls}} \Sigma_{\text{crit}, \text{ls}}}{\sum_{\text{ls}} W_{\text{ls}}}. \quad (4)$$

Here the factor $(1+\mu)$ corrects for the ‘multiplicative bias’ (Fenech Conti et al. 2017). Extending the method of Dvornik et al. (2017) to the higher KiDS-DR4 redshifts, μ is calculated from the multiplicative bias corrections m of the individual sources:

$$\mu = \frac{\sum_s w_s m_s}{\sum_{\text{ls}} w_s}, \quad (5)$$

in 11 linear redshift bins between $0.1 < z_B < 1.2$. The value of this correction is $\mu \approx 0.014$, independent of the projected distance from the lens. After correction, the effects of the multiplicative bias are reduced to $< 1\%$.

We also correct our lensing signal for effects from residual shape correlations due to the (small) PSF anisotropy of the KiDS observations. At the survey edges, it is possible that the averaging of the source shapes is not performed over all azimuthal angles, which can result in systematic effects on the ESD at larger scales ($R > 1 h^{-1}\text{Mpc}$). We correct for this by subtracting the ESD profile measured around random coordinates. From the basic random catalogue created for the KiDS survey, we use a randomly selected sample of ~ 5 million coordinates, which is 50 times the size of our total GL-KiDS sample. These random coordinates mimic the exact footprint of KiDS, including the areas masked by the ‘9-band no AW-*r*-band’ mask which was also applied to the GL-KiDS lenses (see Sect. 2.3). In order to create random redshift values that mimic the true distribution, we create a histogram of the GL-KiDS redshifts divided into 100 linear bins between $0 < z_{\text{ANN}} < 0.5$. In each bin, we create random redshift values equal to the number of real lenses in that bin. We find that the resulting random lensing signal is very small, with a mean absolute value of only $\sim 3\%$ of the lensing signal of the GL-KiDS galaxies. Because of the large contiguous area of KiDS-DR4, the random ESD profile is consistent with zero at all projected radii R .

The error values on the ESD profile are estimated by the square-root of the diagonal of the analytical covariance

matrix, which is described in Sect. 3.4 of Viola et al. (2015). The full covariance matrix is calculated based on the contribution of each individual source to the ESD profile, and incorporates the correlation between sources that contribute to the ESD in multiple bins, both in projected distance R and stellar mass M_* .

The GGL method described above is basically identical to the procedure used by recent KiDS-GGL papers, specifically: Dvornik et al. (2017, 2018) and Brouwer et al. (2017, 2018). For more details on the KiDS-GGL procedure, we recommend reading these recent works. The method that was used in older works (Viola et al. 2015; Sifón et al. 2015; van Uitert et al. 2016; Brouwer et al. 2016) is also very similar, although small changes have occurred in the pipeline with the arrival of new data-releases.

Note that we use the unadulterated GGL method throughout this work, also when testing the MOND and EG theories. We recognize that, by using the basic GGL equations to measure the (apparent) density distributions in these frameworks, we necessarily assume that the laws of GR hold with respect to the deflection of light by a gravitational potential. We therefore motivate in Sect. 5.1 and 5.2 why this assumption holds for the alternative gravity theories we test in this work.

3.2 Isolated galaxy selection

After performing the measurement of the RAR using GGL, our final goal is to compare the results to different analytical models (see Sect. 5) and N-body simulations (see Sect. 2.4 and 2.5) which make specific predictions on the galaxy-halo connection. While the simulations are designed to describe galaxies in their cosmological environment, the analytical models mainly focus on the description of individual galaxies. This means that, in order to test these models, we need to select galaxies that are relatively isolated. Most importantly, their measured ESD profiles should not be significantly affected by neighbouring galaxies, which we will call ‘satellites’. We define our isolated lenses such that they not have any satellites with more than a fraction $f_{M_*} \equiv M_{*,\text{sat}}/M_{*,\text{lens}}$ of their stellar mass, within a spherical radius r_{sat} . We choose $f_{M_*} = 0.1$ which corresponds to 10% of the lens stellar mass, and $r_{\text{sat}} = 3 h^{-1} \text{Mpc}$ which is equal to the maximum projected radius of our measurement. In short: $r_{\text{sat}}(f_{M_*} > 0.1) > 3 h^{-1} \text{Mpc}$. We also restrict our lens stellar masses to $\log(M_*) < 11 h^{-2} M_\odot$, since galaxies with higher masses have significantly more satellites (see Sect. 2.2.3 of Brouwer et al. 2017).

We validate our isolation criterion using the GL-KiDS data and -MICE datasets. Tests with higher values of r_{sat} do not yield any decrease in the 2-halo term: the GGL signal at larger ($> 1 h^{-1} \text{Mpc}$) scales, corresponding to the contribution of satellites. This is true both when all lens masses are considered, and when they are restricted to a specific stellar mass ($\log(M_*) = 10.5 \pm 0.1 h^{-2} M_\odot$). Using lenses with this same stellar mass we perform a test where we reduce the satellite mass fraction to $f_{M_*} = 0$ (corresponding to no visible satellites). This also yields no decrease in the 2-halo term of the ESD profile. When we restrict the total stellar mass M_{tot} of all satellites within r_{sat} to $f_{M_{\text{tot}}} < 0.1$ this does not significantly affect the isolated lens sample (i.e. the samples selected with KiDS are $> 99\%$ overlapping), because

galaxies with $f_{M_*} \ll 0.1$ are not likely to be observed in a flux-limited survey. Finally, we apply our isolation criterion to the GAMA survey, to compare our selected isolated sample with the ‘isolated centrals’ that were used by Brouwer et al. (2017). In that work we used a more elaborate isolation criterion, which was driven by the Friends-of-Friends (FoF) group finding algorithm of Robotham et al. (2011). We find that the two isolated galaxy samples are more than 80% overlapping.

However, because both the GAMA survey and the GL-KiDS and -MICE samples designed to mimic it are flux-limited, satellites that are fainter than the flux limit are not detected. This can cause lenses that are close to the magnitude limit ($m_{\text{lim}} = 20 \text{ mag}$) to be falsely identified as isolated. This problem is illustrated in Fig. 1, which shows that the fraction of galaxies assigned to the isolated lens sample increases for higher values of the apparent r -band magnitude m_r . The dashed vertical line represents the magnitude m_{bright} , below which all satellites with a luminosity fraction larger than $f_L \equiv L_{\text{sat}}/L_{\text{lens}} = 0.1$ compared to the lens are still detected. In the case of GL-KiDS:

$$m_{\text{bright}} < m_{\text{lim}} - 2.5 \log_{10}(f_L = 0.1) < 17.5 \text{ mag}. \quad (6)$$

Applying this magnitude cut provides us with an isolated lens sample that is relatively free of false candidates, allowing us to estimate their effect on the ESD profiles. In Fig. 2 we compare the ESD profiles of isolated galaxies with the more reliable ‘bright’ sample. Due to the smaller number of lenses, the ESD errors and scatter of the bright isolated sample are much larger than those of the full isolated sample. Nevertheless, it is clear that their ESD profiles show consistent behaviour at both small and large scales. Compared to the total (non-isolated) galaxy sample, their small-scale lensing signal (or 1-halo term, corresponding to the lens itself) is increased due to the slightly higher masses of the isolated samples. As expected, their large-scale signal (or 2-halo term, corresponding to the contribution of satellites) is decreased. The high level of consistency between the ESD profiles of the regular and bright isolated galaxies indicates that the effect of false candidates is limited.

Nevertheless, we use the MICE simulations to perform one additional test. We select the isolated sample of GL-MICE lenses using a sample of galaxies that extends to $m_r < 22.5 \text{ mag}$, such that all satellites with $f_L > 0.1$ can be observed. This paints a similar picture as the bright KiDS sample, i.e.: although the much smaller sample of isolated galaxies selected using the faint satellites greatly increases the scatter, we find no consistent decrease in the lensing signal at $> 1 h^{-1} \text{Mpc}$ scales compared to the original sample of isolated GL-MICE galaxies. These tests demonstrate the overall robustness of our isolation criterion. In addition, we note that this issue is only relevant when comparing our observations to the theoretical models (EG, MOND and N17). When comparing to the N-body simulations (BAHAMAS and MICE), applying the same isolation criterion to both data and mocks ensures that any issues with the isolated galaxy selection are mimicked.

The major difference between the isolated galaxy selection of the GAMA and mock galaxies compared to GL-KiDS, is that for GAMA and the mocks the true redshift values are known, whereas the ANNZ photometric redshifts of GL-KiDS are only known within a certain standard deviation σ_z

(see Sect. 2.3). This affects the observed spherical distances r between the galaxies, a key ingredient of the isolation criterion. The redshift uncertainty also affects the GL-KiDS stellar mass estimates, which influences both the isolation criterion (through f_{M_*}) and the application of the stellar mass limit: $\log(M_*) < 11 h^{-2} M_\odot$. We assess the effect of these uncertainties on the isolated galaxy selection by adding a normally distributed random offset with $\sigma_z/(1+z) = 0.018$ to the MICE redshifts, and $\sigma_{M_*} = 0.21$ dex to its stellar masses. We find that the effect of the mass uncertainty is negligible, but that of redshift uncertainty is significant. Because the random redshift offset decreases the galaxy clustering, it increases the number of galaxies selected by the isolation criterion, adding galaxies which are not truly isolated to the lens sample (as well as excluding some truly isolated galaxies). As a result, only 23% of our isolated sample selected using the ‘offset’ MICE data is truly isolated. The ESD profile of the ‘offset’ isolated MICE sample is shown in Fig. 3, compared to the ESD profiles of all MICE galaxies (without any isolation criterion) and the truly isolated MICE sample. At scales $R > 0.3 h^{-1} \text{Mpc}$ the ESD of the isolated sample selected using the ‘offset’ MICE data is $\sim 30\%$ higher than that of the truly isolated MICE galaxies. When comparing our GL-KiDS lensing measurements to the MICE simulation, this effect can easily be taken into account by mimicking the redshift offset in the simulation. However, for our comparison with the analytical models (MOND, EG) and the BAHAMAS simulation, this process is much more difficult. We conclude that we can only use the ESD profile of isolated GL-KiDS lenses within $R < 0.3 h^{-1} \text{Mpc}$. For the mean galaxy mass of the isolated GL-KiDS sample ($\log(M_{\text{gal}}) = 10.67 h^{-2} M_\odot$) this corresponds to a baryonic acceleration of $g_{\text{gal}} > 0.73 \times 10^{-13}$. For each RAR measurement resulting from isolated GL-KiDS lenses we will indicate the range in g_{gal} where the measurement is reliable, based on the mean M_{gal} of the lenses. For the accelerations exceeding this limit, we use the lensing results from the spectroscopic GAMA survey.

4 CONVERSION TO THE RAR

After measuring the lensing profile around a galaxy sample, the next important step is to convert it into the corresponding RAR. We start from the ESD $\Delta\Sigma(R)$ as a function of projected radius R and the measured stellar masses of the lens galaxies M_* , and aim to arrive at their observed radial acceleration g_{obs} as a function of their expected baryonic radial acceleration g_{bar} . The latter can be calculated using Newton’s law of universal gravitation:

$$g(r) = \frac{GM(<r)}{r^2}. \quad (7)$$

which defines the radial acceleration g in terms of the gravitational constant G and the enclosed mass $M(<r)$ within spherical radius r . The calculation of g_{bar} requires the enclosed baryonic mass $M_{\text{bar}}(<r)$ of the galaxies. We discuss our construction of $M_{\text{bar}}(<r)$ in Sect. 4.1.

The calculation of g_{obs} requires the enclosed observed mass $M_{\text{obs}}(<r)$ of the galaxy sample, which we obtain through the conversion of our observed ESD profile $\Delta\Sigma(R)$. To make sure this conversion is robust, we compare two different methods: a simple analytical method which assumes

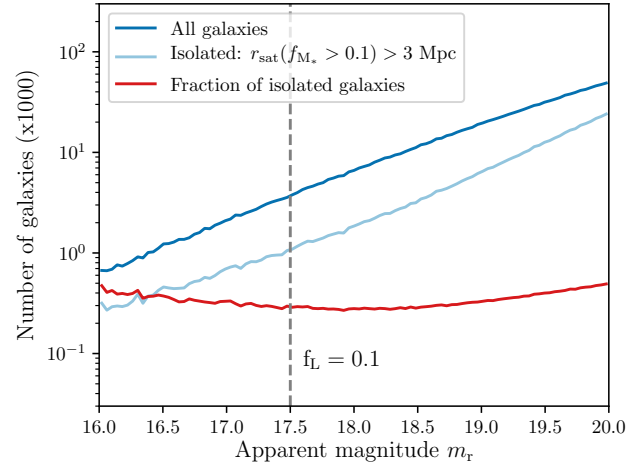


Figure 1. The number of isolated galaxies (light blue) compared to the total number of galaxies (dark blue), as a function of apparent r -band magnitude m_r . The fraction of ‘isolated galaxies’ (red) slightly increases with apparent magnitude, because satellites fainter than the flux limit are not detected, which can cause lenses close to the magnitude limit ($m_{\text{lim}} = 20 \text{ mag}$) to be falsely identified as isolated. The dashed vertical line represents the magnitude m_{bright} , below which all satellites with a luminosity fraction larger than $f_L \equiv L_{\text{sat}}/L_{\text{lens}} = 0.1$ compared to the lens are still detected.

that DM haloes can be roughly approximated with a Singular Isothermal Sphere density model (Sect. 4.2), and an elaborate numerical approach which fits a piece-wise power law to the stacked ESD profile (Sect. 4.3) without any assumption on the averaged halo shape except for spherical symmetry. We validate both methods using mock surface density maps from the BAHAMAS simulation (Sect. 4.4).

4.1 Baryonic mass of the galaxies

The calculation of the expected baryonic radial acceleration g_{bar} requires the enclosed baryonic mass $M_{\text{bar}}(<r)$ within a spherical radius r around the galaxy centre. Since we are dealing with measurements around isolated galaxies ($R > 30 h^{-1} \text{kpc}$), we can approximate $M_{\text{bar}}(<r)$ as a point mass M_{gal} mainly composed of the mass of the lens galaxy itself. M_{gal} can be roughly subdivided into stars and gas, where the latter can be further distinguished into cold and hot gas.

The stellar masses of our GAMA and GL-KiDS galaxies are estimated using their multi-band spectral energy distributions, by fitting them with stellar population synthesis models (see Sect. 2.2 and 2.3). The MICE stellar masses are determined from their luminosities using M/L ratios, and the BAHAMAS stellar masses from their calibrated prescriptions for star formation and stellar evolution (see Sect. 2.4 and 2.5). From these M_* values, the fraction of cold gas $f_{\text{cold}} = M_{\text{cold}}/M_*$ can be estimated using scaling relations based on HI and CO observations. Following Brouwer et al. (2016) we use the best-fit scaling relation found by Boselli et al. (2014), based on the Herschel Reference Survey (Boselli et al. 2010):

$$\log(f_{\text{cold}}) = -0.69 \log(M_*) + 6.63. \quad (8)$$

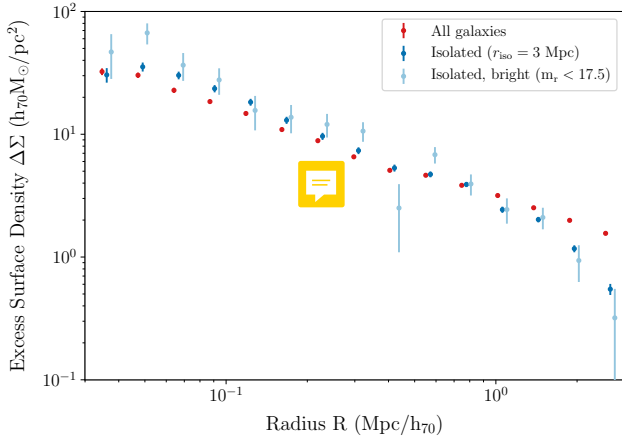


Figure 2. To assess the effect of the magnitude limit ($m_{\text{lim}} = 20$ mag) on the isolation criterion, we compare the ESD profile of the isolated galaxies (dark blue) with that of a more reliable ‘bright’ sample (dark blue, $m_{\text{lim}} < 17.5$ mag), which allows us to see all satellites down to luminosity fraction $f_L \equiv L_{\text{sat}}/L_{\text{lens}} = 0.1$. Due to the smaller number of lenses, the ESD profile of the bright isolated sample shows much larger error bars and scatter. Nevertheless, its behaviour on both small and large scales is consistent with the ESD profile of the full isolated sample, indicating that the effect of the magnitude limit is limited.

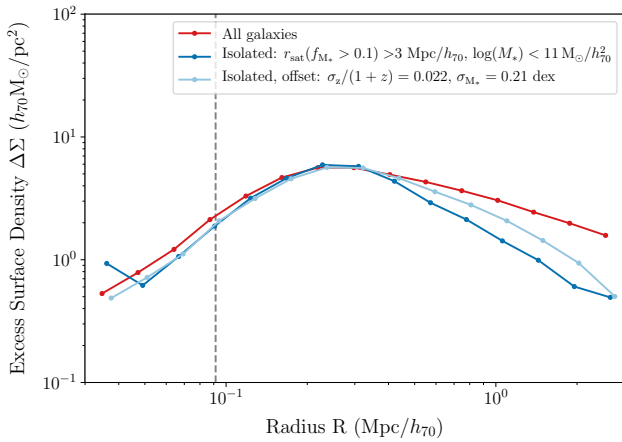


Figure 3. The ESD profile of the ‘offset’ isolated sample of MICE galaxies (light blue) selected using lenses with randomly offset redshifts ($\sigma_z/(1+z) = 0.018$) and stellar masses ($\sigma_{M_*} = 0.21$ dex). Compared to the ESD profile of the truly isolated MICE sample (dark blue) the ‘offset’ sample has a $\sim 30\%$ higher signal at large scales ($R > 0.5 h^{-1}$ Mpc), although it is still significantly lower than that of all MICE galaxies (red).

We apply this equation to all observed and simulated values of M_* in order to arrive at the total galaxy mass: $M_{\text{gal}} = M_* + M_{\text{cold}} = M_*(1 + f_{\text{cold}})$. The spatial distribution of the stellar and cold gas mass are similar (Pohlen et al. 2010; Crocker et al. 2011; Mentuch Cooper et al. 2012; Davis et al. 2013) and can therefore be considered a single mass distribution, especially for the purposes of GGL which only measures the ESD profile at scales larger than the galaxy itself ($R > 30 h^{-1}$ kpc). Fig. 4 shows the enclosed

mass profiles (upper panel) and RAR (lower panel) for different baryonic components in the BAHAMAS simulation. The stellar mass at $30 h^{-1}$ Mpc (red star) gives a good approximation of M_* across all radii (dotted red line). We therefore model the baryonic mass of our galaxies as a point mass M_{gal} , containing both the stellar and cold gas mass.

However, the total baryonic mass distribution M_{bar} including hot gas can extend to much larger distances. This is shown in blue in Fig. 4, where the upper limit is given by the BAHAMAS simulation (dark blue line) and the lower limit by ... observations from Tumlinson et al. (2017) (bottom of the light blue band). The region in between these lines (light blue band) represents the so-called ‘missing baryons’ (Fukugita et al. 1998; Fukugita & Peebles 2004; Shull et al. 2012), which are currently thought to reside in the difficult to observe Warm-Hot Intergalactic Medium (WHIM, Nicastro et al. 2018). This missing mass is predicted by Big Bang Nucleosynthesis (BBN, Kirkman et al. 2003) and CMB measurements (Spergel et al. 2003; Planck XVI 2014), but can not normally be observed by multi-wavelength surveys. Our analysis can therefore not constrain the contribution to g_{bar} based on this component, although a hard upper limit at sufficiently large radii is given by the cosmic baryon fraction $f_b = \Omega_b/\Omega_m = 0.17$ (Hinshaw et al. 2013), which is shown in yellow. Given this inherent inability, we will use the galaxy mass M_{gal} as our best estimate of the total baryonic mass M_{bar} , which we use to compute the baryonic acceleration g_{bar} throughout this work. We note, however, that even if the stellar+cold gas mass is not a good approximation of the total baryonic mass within $3 h^{-1}$ Mpc, this will not affect the comparison between our GGL observations and the different DM simulations/MG models as long as all these predictions are based only on the mass M_{gal} of the galaxy (which is the case in this work).

Concerning predictions within the Λ CDM framework, omitting the use of hot gas will not affect our models since the total mass distribution at the considered scales ($> 30 h^{-1}$ kpc) is dominated by DM. Within a modified gravity framework such as EG and MOND, where the excess gravity emanates from the baryonic matter, it is slightly more complicated. In Sect. 2.2 of Brouwer et al. (2016) we carefully modelled the distribution of all baryonic components, based on observations from both GAMA and literature, including their effect on the excess gravity. We found that, for galaxies with $M_* < 1 \times 10^{11} h^{-2} M_{\odot}$, the contribution to the ESD profile from hot gas and satellites was small compared to that of the stars and cold gas. Although this analysis was done for the EG theory, the effect of these extended mass distributions within MOND are similar or even less. This allows us to use a point mass M_{gal} as a reasonable approximation for the baryonic mass distribution $M_{\text{bar}}(< r)$ within our measurement range when computing the predictions of EG and MOND (see Sect. 5.2 and 5.1).

4.2 Singular Isothermal Sphere approximation

When calculating g_{obs} we start out from our ESD profile measurement, which consists of the value $\Delta\Sigma(R)$ measured in a set of R -bins. At our measurement radii ($R > 30 h^{-1}$ kpc) the ESD is dominated by the DM halo. We can therefore adopt the simple assumption that our observed density profile $\rho_{\text{obs}}(r)$ is roughly described by a Singular

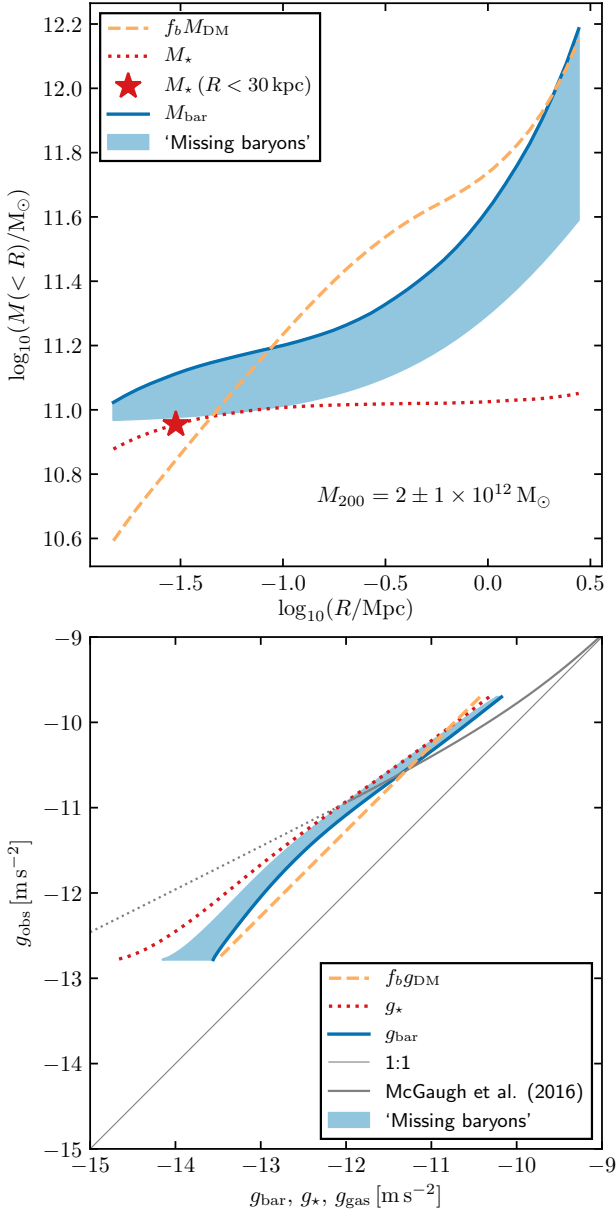



Figure 4. *Upper panel:* Cumulative mass profiles of stars (dotted red) and baryons (solid blue) for BAHAMAS galaxies with $1 < M_{200}/10^{12}M_{\odot} < 3$. The star marker indicates the stellar mass within a 30 kpc aperture, indicative of what is typically regarded as the stellar mass of a galaxy. The blue shaded band shows an estimate based on fig. 7 of Tumlinson et al. (2017) of the baryonic mass which would be ‘missing’ in even a multi-wavelength survey. In the  galaxy only a small fraction of the baryons are missing, but in the outer galaxy the majority are missing. The yellow dashed line shows the expected baryonic mass profile if the baryon density is everywhere equal to a fixed fraction $f_b = \Omega_b/\Omega_m$ of the local dark matter density. At large enough radii ($\gtrsim 2$ Mpc), the baryon-to-DM ratio converges to the cosmic average. *Lower panel:* As in upper panel, but in acceleration space. The cosmic baryon fraction provides a robust upper limit on g_{bar} at low accelerations.

Isothermal Sphere (SIS) model:

$$\rho_{\text{SIS}}(r) = \frac{\sigma^2}{2G\pi r^2}. \quad (9)$$

The SIS is generally considered to be the simplest parametrization of the spatial distribution of matter in an astronomical system (such as galaxies, clusters, etc.). It assumes that the dominant constituent particles (in our case DM) behave as an ideal gas that is confined by their combined spherically symmetric gravitational potential, where σ is the total velocity dispersion of the particles. Despite its simple form, the ESD derived from the SIS profile:

$$\Delta\Sigma_{\text{SIS}}(R) = \frac{\sigma}{2GR}, \quad (10)$$

is generally able to describe WL measurements around galaxies and clusters (references). The SIS profile is therefore ideally suited to model the total enclosed mass distribution of our lenses, which can then be derived as follows:

$$M_{\text{SIS}}(<r) = 4\pi \int_0^r \rho_{\text{SIS}}(r') r'^2 dr' = \frac{2\sigma^2 r}{G}. \quad (11)$$

Now, for each measured value of $\Delta\Sigma_{\text{obs}}$ at its projected radius R , we assume that the entire density profile is described by a SIS with σ normalized such that $\Delta\Sigma_{\text{SIS}}(R)$ goes through $\Delta\Sigma_{\text{obs}}$. We also assume that the considered lens is flat, in order to approximate the spherical distance r with the measured transverse distance R . Using these assumptions, we can combine Eq. 10 and 11 to compute the observed enclosed mass distribution corresponding to that measurement:

$$M_{\text{obs}} = \frac{2(2GR\Delta\Sigma)r}{G} = 4\Delta\Sigma r^2. \quad (12)$$

Through Eq. 7, this results in a very simple expression for the observed gravitational acceleration:

$$g_{\text{obs}} = \frac{G(4\Delta\Sigma r^2)}{r^2} = 4G\Delta\Sigma, \quad (13)$$

computed at each point along the ESD profile.

4.3 Piece-wise power law density profile

We can instead assume a more self-consistent form for the volume density profile and parametrize it as a piece-wise power law constrained to be continuous. This comes at the cost of needing to invert the non-linear function $\Delta\Sigma(\rho)$, which we achieve via an iterative method. We choose to parametrize $\rho(r)$ in terms of N pairs of values (r_n, ρ_n) such that the slope a_n and normalization b_n of the power law profile segments are:

$$\log \rho = a_n \log(r) + b_n \quad (14)$$

$$a_n = \frac{\log(\rho_{n+1}) - \log(\rho_n)}{\log(r_{n+1}) - \log(r_n)} \quad (15)$$

$$b_n = \log(\rho_n) - a_n \log(r_n) \quad (16)$$

$$(a_n, b_n) = \begin{cases} (a_0, b_0) & \text{if } r < r_0 \\ (a_n, b_n) & \text{if } r_n \leq r < r_{n+1} \\ (a_{N-1}, b_{N-1}) & \text{if } r \geq r_N \end{cases} \quad (17)$$

(Throughout, \log denotes the natural logarithm.) We provide an expression for the discrete excess surface density

profile in terms of the volume density profile, i.e. the function to be inverted, in Appendix A.

In order to invert $\Delta\Sigma_m(\rho_n)$, we take as constant the values $\{R_m\}$, $\{\Delta\Sigma_m\}_{\text{obs}}$ and $\{r_n\}$. We then propose an initial guess $\{\rho_n\}$ which we perturb iteratively, calculating the corresponding $\{\Delta\Sigma_m\}$ at each iteration and comparing with $\{\Delta\Sigma_m\}_{\text{obs}}$ via the likelihood function:

$$\log \mathcal{L} \propto -\frac{1}{2}(\Delta\Sigma_{\text{obs}} - \Delta\Sigma)^T C^{-1}(\Delta\Sigma_{\text{obs}} - \Delta\Sigma) \quad (18)$$

where C is the covariance matrix for the $\Delta\Sigma_{\text{obs}}$. We use the package EMCEE (Foreman-Mackey et al. 2013) to estimate the posterior probability distribution of $\{\rho_n\}$, and subsequently of the corresponding $\{g_{\text{obs},n}\}$ via integration of the volume density profile.

4.4 Testing the RAR conversion with BAHAMAS

[This section just notes so far, proper write-up to follow.] The PPL method underestimates the enclosed mass within all radii, in this example. Part of the offset is due to the difference between the $\Delta\Sigma$ profile as determined from spherical shells (red line in Fig. 5, left panel) and that determined from the mock convergence maps (yellow line in Fig. 5, left panel). The difference is nearly constant with radius and so enters as an overall normalization constant, and the same constant appears in both the expression for the excess surface density and that for the enclosed mass: therefore the ~ 0.05 dex offset in the $\Delta\Sigma$ accounts for ~ 0.05 dex of the offset in enclosed mass, i.e. most of the offset at large radii. The additional missing mass at small radii is because the slope inside the innermost measured radius is very difficult to constrain. In this case, the preferred power law slope for $\rho(r)$ – which gets extrapolated to $r = 0$ – is -1.4 . An inner slope of -2.1 would increase the central mass up to a deficit of 0.05 dex, i.e. enough to be consistent with the offset of the outermost points. But note that the method does a good job of reflecting the difficulty in constraining the inner slope in the error estimates, which increased significantly toward the centre.

The SIS method appears to do better at the innermost radius. This success is explained by the fact that the ‘effective power law slope’ (given the correct normalization) of $\rho(r)$ inside the innermost radius is -2.1 , as explained above – thus assuming a slope of -2.0 turns out to be a pretty good approximation. The slight deficit at the innermost radius is accounted for by the slight underestimate of the slope and once again by the difference between the $\Delta\Sigma$ profile obtained from the mock convergence maps and that obtained from spherical shells. The success continues while the slope remains close to -2 – until about 300 kpc. Beyond this the estimate gradually increases relative to the truth, as the slope estimate is increasingly an overestimate. The visually good agreement is actually a happy coincidence, resulting from an approximate cancellation between the $\Delta\Sigma$ normalization offset and the slope overestimate.

The offset between the mock convergence map-derived $\Delta\Sigma$ and the one derived from spherical shells seems to be systematic – it persists in any BAHAMAS mock sample I choose. The magnitude of the offset seems to vary between about -0.05 dex and -0.10 dex. I think this depends on the amount of substructure. Imagine a spherically symmetric

system and its corresponding surface density map. Now remove a bit of mass from the spherical average and instead put it into a localized substructure at the same radius. The surface density of a few pixels at the location of the substructure will go up a lot, while the surface density of many pixels everywhere else at the same radius will go down a little bit. Depending on how the pixels are combined (more like a median or mean) it’s plausible that the case with substructure results in a systematic underestimate of the surface density profile, and therefore the ESD profile.

The poor match with the M16 result in the right panel of Fig. 5 is most likely due to the limited spatial resolution of BAHAMAS – need to look into this further. Should highlight that the plot here is g_* and not g_{bar} .

5 THEORETICAL PREDICTIONS

5.1 Modified Newtonian Dynamics

With his theory of Modified Newtonian Dynamics (MOND), Milgrom (1983) postulated that the ‘missing mass problem’ in galaxies is not caused by an undiscovered fundamental particle, but that instead our current gravitational theory should be revised. MOND’s basic premise is that one can adjust Newton’s second law of motion ($F = ma$) by inserting a general function $\mu(a/a_0)$, which only comes into play when the acceleration a of a test mass m is much smaller than a critical acceleration a_0 . The goal of this function is to facilitate the discovered flat rotation curves in the outskirts of galaxies, while still reproducing the Newtonian behaviour of the inner disk. In short, the force F becomes:

$$F(a) = m \mu\left(\frac{a}{a_0}\right) a, \quad \mu(x \gg 1) \approx 1, \quad \mu(x \ll 1) \approx x. \quad (19)$$

This implies that $a \gg a_0$ represents the Newtonian regime where $F_N = m a_N$ as expected, while $a \ll a_0$ represents the ‘deep-MOND’ regime where $F_{\text{dm}} = m a_{\text{dm}}^2/a_0$. In a circular orbit, this is reflected in the deep-MOND gravitational acceleration $g_{\text{dm}} \equiv a_{\text{dm}}$ as follows:

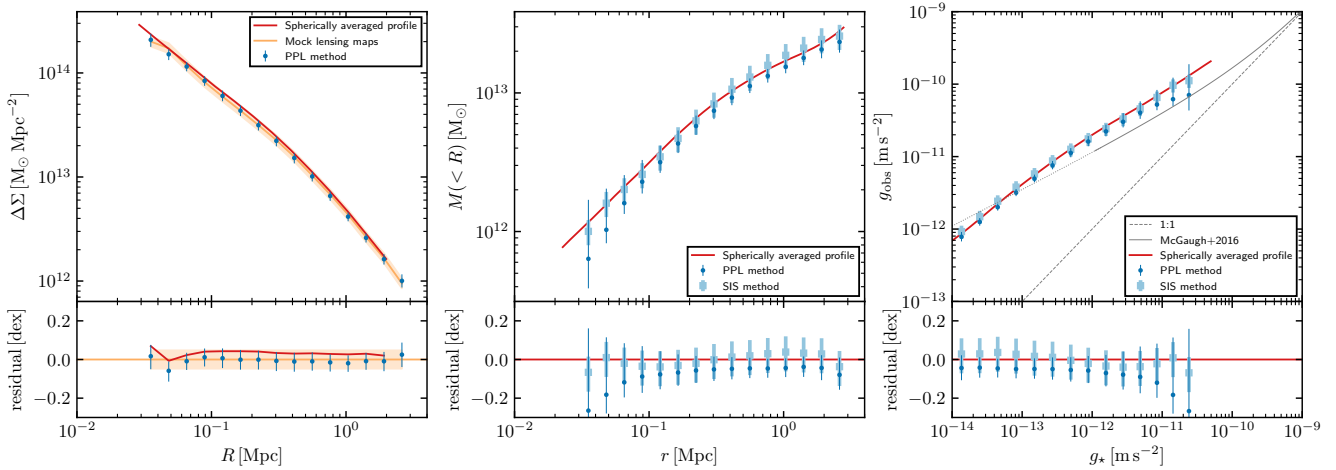
$$F_{\text{dm}} = m \frac{a_{\text{dm}}^2}{a_0} = \frac{G M m}{r^2} \rightarrow g_{\text{dm}} = \sqrt{a_0 \frac{G M}{r^2}}. \quad (20)$$

This can be written in terms of the expected baryonic acceleration $g_{\text{bar}} = G M/r^2$ as follows:

$$g_{\text{dm}}(g_{\text{bar}}) = \sqrt{a_0 g_{\text{bar}}}, \quad (21)$$

which demonstrates that MOND predicts a very simple relation for the RAR: $g_{\text{obs}} = g_{\text{bar}}$ in the Newtonian regime ($g_{\text{obs}} \gg a_0$), and following Eq. 20 in the deep-MOND regime ($g_{\text{obs}} \ll a_0$). However, since $\mu(a/a_0)$ (also known as the ‘interpolating function’) is not specified by Milgrom (1983), there is no specific constraint on the behaviour of this relation in between the two regimes. In the work of Milgrom & Sanders (2008), several families of interpolation functions are discussed. Selecting the third family (given by their Eq. 13) with constant parameter $\alpha = 1/2$, provides the function that M16 later used to fit to their measurement of the RAR using rotation curves 153 galaxies. This relation can be written as:

$$g_{\text{obs}} = \frac{g_{\text{bar}}}{1 - e^{-\sqrt{g_{\text{bar}}/a_0}}}. \quad (22)$$

Figure 5. *To be written.*

where $a_0 \equiv g_{\dagger}$ corresponds to the fitting parameter constrained by M16 to be $g_{\dagger} = 1.20 \pm 26 \times 10^{-10} \text{ m/s}^2$. Since Eq. 22 (equal to Eq. 4 in M16) is also considered a viable version of the MOND interpolation function by [Milgrom & Sanders \(2008\)](#), we will consider it the baseline prediction of MOND in this work. As the baseline value of a_0 , we will likewise use the value of g_{\dagger} measured by M16, since it exactly corresponds to the value of $a_0 = 1.2 \times 10^{-10} \text{ m/s}^2$ considered canonical in MOND since its first measurement by [Begeman et al. \(1991\)](#), using the rotation curves of 10 galaxies.

5.2 Emergent Gravity

The work of [Verlinde \(2016\)](#) (V16 hereafter), which is embedded in the framework of string theory and holography, shares the view that the missing mass problem is to be solved through a revision of our current gravitational theory. Building on the ideas of [Jacobson \(1995, 2016\)](#); [Padmanabhan \(2010\)](#); [Faulkner et al. \(2014\)](#) and his own previous work ([Verlinde 2011](#)), V16 abandons the notion of gravity as a fundamental force. Instead, it emerges from an underlying microscopic description of space-time, in which the notion of gravity has no a-priori meaning.

The aforementioned earlier works have shown that constructing a theory EG in a static (‘anti-de Sitter’) universe allows for the re-derivation Einstein’s laws of GR. A distinguishing feature of V16 is that it attempts to describe an expanding (‘de Sitter’) universe, which is filled with a DE component. This results in a new volume law for gravitational entropy caused by DE, in addition to the area law normally used to retrieve Einsteinian gravity. According to V16, energy that is concentrated in the form of a baryonic mass distribution causes an elastic response in the entropy of the surrounding DE. This results in an additional gravitational component at scales set by the ‘Hubble acceleration scale’ $a_0 = cH_0$. Here c is the speed of light, and H_0 is the current Hubble constant which measures the Universe’s expansion velocity.

Because this extra gravitational component is predicted to explain the effects usually attributed to DM, it is often

expressed as an *apparent* dark matter (ADM) distribution:

$$M_D^2(r) = \frac{cH_0 r^2}{6G} \frac{d(M_b(r)r)}{dr}. \quad (23)$$

Thus the ADM distribution is completely defined by the baryonic mass distribution $M_b(r)$ as a function of the spherical radius r , and a set of known physical constants.

Since we measure the ESD profiles of galaxies at projected radial distances $R > 30 h_{70}^{-1} \text{ Mpc}$, we can assume that their baryonic component is enclosed within the minimal measurement radius (see also [Brouwer et al. 2017](#)). This is equivalent to describing the galaxy as a point mass M_b , which allows us to simplify Eq. 23 to:

$$M_D(r) = \sqrt{\frac{cH_0 M_b}{6G}} r. \quad (24)$$

Now the total enclosed mass, $M_{EG}(r) = M_b + M_D(r)$, can be used to calculate the predicted gravitational acceleration $g_{EG}(r)$ as follows:

$$g_{EG}(r) = \frac{GM_{EG}(r)}{r^2} = \frac{GM_b}{r^2} + \sqrt{\frac{cH_0}{6}} \frac{\sqrt{GM_b}}{r}. \quad (25)$$

In terms of the expected baryonic acceleration $g_{bar}(r) = GM_b/r^2$, this simplifies even further to:

$$g_{EG}(g_{bar}) = g_{bar} + \sqrt{\frac{cH_0}{6}} \sqrt{g_{bar}}. \quad (26)$$

Note that Eq. 23 is only a macroscopic approximation of the underlying microscopic phenomena described at the start of this section, and is thus only valid for static, spherically symmetric and isolated baryonic mass distributions. For this reason, we select only the most isolated galaxies from our sample (see Sect. 3.2), such that our WL measurements are not influenced by neighbouring galaxies. In addition, cosmological evolution of the H_0 parameter is not yet implemented in the theory, restricting its validity to galaxies with relatively low redshifts. However, we calculate that at our mean lens redshift ($\langle z \rangle \sim 0.2$) using an evolving $H(z)$ would result in only a 5% difference in our ESD measurements, based on the background cosmology used in this work.

In order to test V16 using the standard WL methodology, we need to assume that the deflection of photons by a gravitational potential in this alternative theory corresponds to that in GR. This assumption is justified because, in EG’s original (anti-de Sitter) form, Einstein’s laws emerge from its underlying description of space-time. The additional gravitational force described by ADM does not affect this underlying theory, which is an effective description of GR. Therefore, we assume that the gravitational potential of an ADM distribution produces the same lensing shear as an equivalent distribution of actual matter.

5.3 Analytical CDM model

To help guide an intuitive interpretation of the lensing RAR within the framework of the Λ CDM theory, we make use of the simple model of N17 which combines a basic model of galactic structure and scaling relations to predict the RAR. We refer to N17 for a full description, but give a summary here. A galaxy of a given stellar (or baryonic – there is no distinction in this model) mass occupies a dark matter halo of a mass fixed by the abundance matching relation of Behroozi et al. (2013). The dark halo concentration is fixed to the cosmological mean for haloes of that mass (Ludlow et al. 2014). The baryonic disc follows an exponential surface density profile with a half-mass size fixed to $0.2 \times$ the scale radius of the dark halo (N17). The above is sufficient to specify the cumulative mass profile of both the baryonic and dark components of the model galaxy; calculating g_{obs} and g_{bar} is then straightforward.

6 RESULTS

We apply the isolation criterion to the lens galaxy samples ($r_{\text{sat}}(f_{M_*} > 0.1) > 3 h^{-1} \text{Mpc}$, see Sect. 3.2), measure their ESD profiles (Sect. 3.1) and convert these into the RAR (Sect. 4). The same procedure is applied to the mock lens samples from MICE and BAHAMAS in order to obtain the prediction from Λ CDM simulations, while the predictions from MOND, EG and the N17 CDM model are calculated analytically based on the average baryonic mass of each lens galaxy sample. In this section we show the results of the lensing RAR measurements, and compare these to the respective predictions. As a reference, we always show the M16 RAR measurement from galaxy rotation curves.

6.1 Comparison to analytical models

In the following subsections, we compare our results to the predictions of the analytical modified gravity models MOND and EG (described in Sect. 5.3 and 5.1), and the N17 analytical CDM model (described in Sect. 5.2).

6.1.1 Isolated GAMA and GL-KiDS galaxies

In Fig. 6 we show the lensing RAR measured using the GAMA and GL-KiDS isolated lens samples. Due to its smaller survey area (180 vs. 1006 deg^2), the error bars using GAMA lenses are larger than those using GL-KiDS lenses.

However, as explained in Sect. 3.2, the spectroscopic redshifts of the GAMA survey allow for a much more reliable selection of the isolated lenses compared to KiDS, which measures photometric redshifts with a $\sigma_z = 0.018$ uncertainty. The effect of this uncertainty on the measured lensing profiles is modelled in Fig. 3, which shows that the ESD profile of the ‘offset’ MICE sample diverges from the truly isolated MICE galaxies at radius $R > 0.3 h^{-1} \text{Mpc}$. We translate this radius into a gravitational acceleration value using Eq. 7, based on the average M_{bar} of the lens sample. In this way we estimate that, for the isolated GL-KiDS galaxies, the isolation criterion is reliable within $g_{\text{bar}} \lesssim 10^{-13}$, as shown by the blue dotted vertical line. Beyond this line (blue shaded region) the effect of satellite galaxies on the lensing signal can result in systematically higher values of g_{obs} , due to the possible contribution of satellite galaxies. The grey band shows the range of possible bias due to a $\Delta M_* = 0.2 \text{ dex}$ systematic shift in stellar mass, which we estimate by performing our analysis assuming stellar masses that are 0.2 dex higher/lower than their best-fit M_* values (see Sect. 2.3). We only show this band once, for the GL-KiDS result, but note that this bias equally affects the GAMA stellar masses (and, indeed, any stellar mass measurement; see e.g. Wright et al. 2017).

Alongside our results we show the M16 RAR measurements (both the mean and 2D histogram) from galaxy rotation curves, which cover higher accelerations (corresponding to smaller scales: $R < 30 h^{-1} \text{kpc}$) than our lensing measurements. At the highest acceleration end (smallest scales), where g_{obs} is dominated by g_{bar} , it follows a one-to-one relation (grey dotted line). Their results quickly diverge from unity at lower accelerations (larger scales), signifying the DM dominated regime. It is very reassuring that, although we use two completely different methods to measure the RAR, our results overlap perfectly between $10^{-12} < g_{\text{bar}} < 10^{-11} \text{ m/s}^2$ (corresponding to $R \sim 30 h^{-1} \text{kpc}$). In this section we compare the two modified gravity models, EG and MOND to our lensing results (for a comparison of these two models with the M16 rotation curves, see Lelli et al. 2017). As explained in Sect. 5.1 we take the MOND prediction to be equal to the extrapolated M16 fitting function (Eq. 22), and that of EG as Within our measurement range, the two predictions are almost indistinguishable. Both models appear to be compatible with the GAMA data, while the GL-KiDS data-points lie systematically above the predictions. However, this could be caused by the contribution of satellites due to the mentioned uncertainty in the photometric GL-KiDS redshifts, especially at accelerations $g_{\text{bar}} < 10^{-13}$. The mentioned 0.2 dex stellar mass bias can also alleviate this tension (but only if it happens to be in the right direction).

To quantify our findings, we compare the predicted g_{mod} of the model with the observed g_{obs} by calculating the χ^2 value:

$$\chi^2 = (g_{\text{obs}} - g_{\text{mod}})^T \cdot C^{-1} (g_{\text{obs}} - g_{\text{mod}}). \quad (27)$$

where C^{-1} is the inverse of the analytical covariance matrix (see Sect. 3.1). We divide this quantity by the number of degrees of freedom N_{DOF} of the model, which gives us the reduced χ^2 statistic:

$$\chi^2_{\text{red}} = \frac{\chi^2}{N_{\text{DOF}}} = \frac{\chi^2}{N_{\text{data}} - N_{\text{param}}}, \quad (28)$$

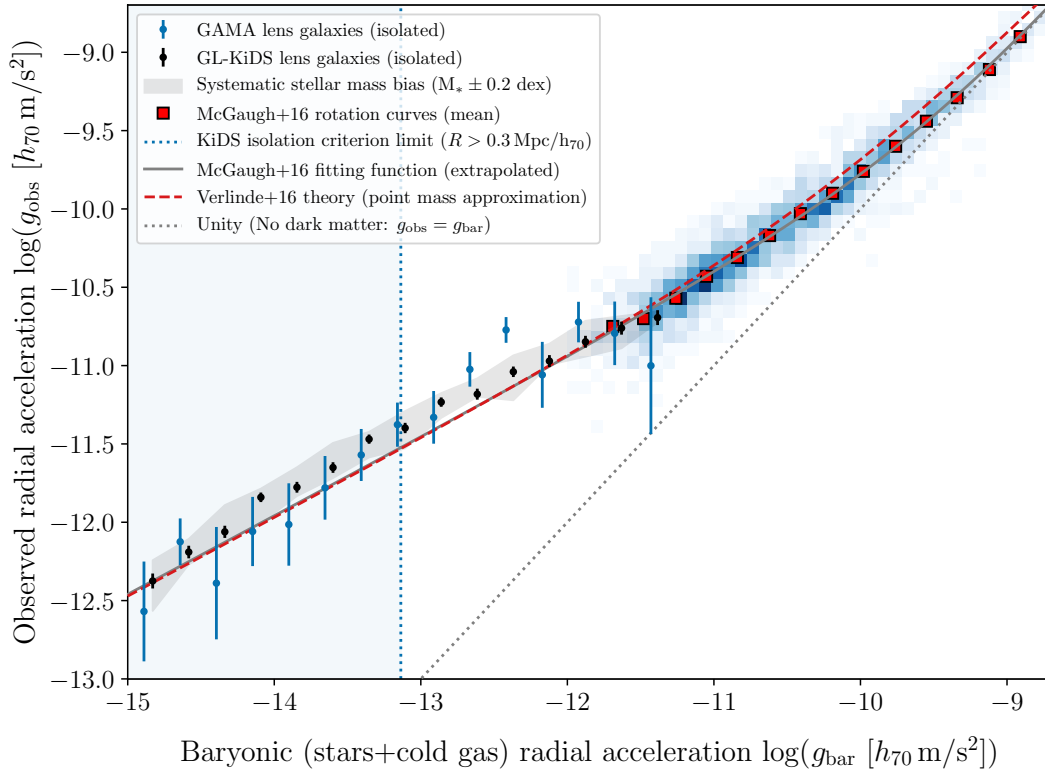


Figure 6. The RAR is defined as the measured total gravitational acceleration g_{obs} (y-axis) and the expected baryonic acceleration g_{bar} (x-axis) of galaxies. At high accelerations (corresponding to small scales) we show the M16 RAR measurements from galaxy rotation curves (binned data in blue, mean in red squares). With lensing we are able to extend this measurement to lower accelerations, using both the spectroscopic GAMA (blue dots with error bars) and the photometric GL-KiDS (black dots with error bars) isolated lens samples. For the GL-KiDS sample, we also show the possible range resulting from a systematic stellar mass bias of $\Delta M_* = 0.2$ dex (grey band). We compare our lensing observations to two modified gravity models: MOND (the M16 fitting function; grey solid line) and EG (assuming a point mass; red dashed line). The GAMA results appear to be in agreement with the two models, while those from GL-KiDS seem systematically higher. However, especially at very low accelerations (corresponding to $R > 0.3 h^{-1} \text{Mpc}$; blue dotted line) the uncertainty in the photometric KiDS redshifts affects the isolated lens selection, resulting in systematically higher values of g_{obs} due to the possible contribution of satellites.

Here N_{data} is the number of data-points in the measurement and N_{param} is the number of free parameters in the model. Since none of the models have free parameters, N_{DOF} is simply the number of g_{bar} -bins (in this case $N_{\text{data}} = 15$).

Comparing the GAMA data to the two modified gravity models results in χ^2_{red} -values of 1.28 for MOND and 1.30 for EG, corresponding to a standard deviation of 1.27 and 1.31σ respectively. This confirms that both models agree well with the GAMA data, with a slight advantage for the MOND prediction. Using the GL-KiDS results however, both models perform much worse: $\chi^2_{\text{red}} = 7.82$ and 8.63 for MOND and EG respectively. Taking into account the effect of the photo- z uncertainty of GL-KiDS by only using the $N_{\text{data}} = 7$ points within the isolation criterion limit ($R < 3 h^{-1} \text{Mpc}$) results in slightly better values: $\chi^2_{\text{red}} = 50.05/7 = 7.15$ for MOND and $\chi^2_{\text{red}} = 54.28/7 = 7.75$ for EG, although this is still almost 6σ away from a good fit. Of course there is still the possible $\Delta M_* = 0.2$ dex bias in stellar mass, shown by the grey band. If this would shift the data downward, the χ^2_{red} of MOND could be as low as 2.97 (with data-points beyond the isolation criterion limit still removed). If it shifts the data upward, however, this χ^2_{red} could be as high as 29.20 . This indicates that GGL measurements are now so accurate

in determining the total observed mass, that improving the RAR measurement would primarily come down to getting a better handle on the baryonic mass distribution.

6.1.2 GL-KiDS galaxies in 4 stellar mass bins

One of the main characteristics of the MOND paradigm, is that it gives a direct and fixed prediction for the total acceleration based only on that of baryonic mass, given by Eq. 22. Since the RAR is the observation of exactly this relation, in principle it should remain fixed independent of any other galaxy characteristics (except perhaps through the External Field Effect). For EG the prediction can deviate from Eq. 26 depending on the slope of the baryonic mass distribution, but at the scales we observe ($R > 30 h^{-1} \text{kpc}$) we found that the prediction for an extended isolated galaxy distribution does not significantly differ from a prediction that assumes the galaxy to be a point mass within $R = 30 h^{-1} \text{kpc}$ (see Sect. 4.3 of Brouwer et al. 2017). Thus, given their current predictions, both models predict approximately the same fixed RAR (at the relevant acceleration scale: $g_{\text{bar}} < 10^{-11}$). The large size of the GL-KiDS lens sample gives us the opportunity to di-

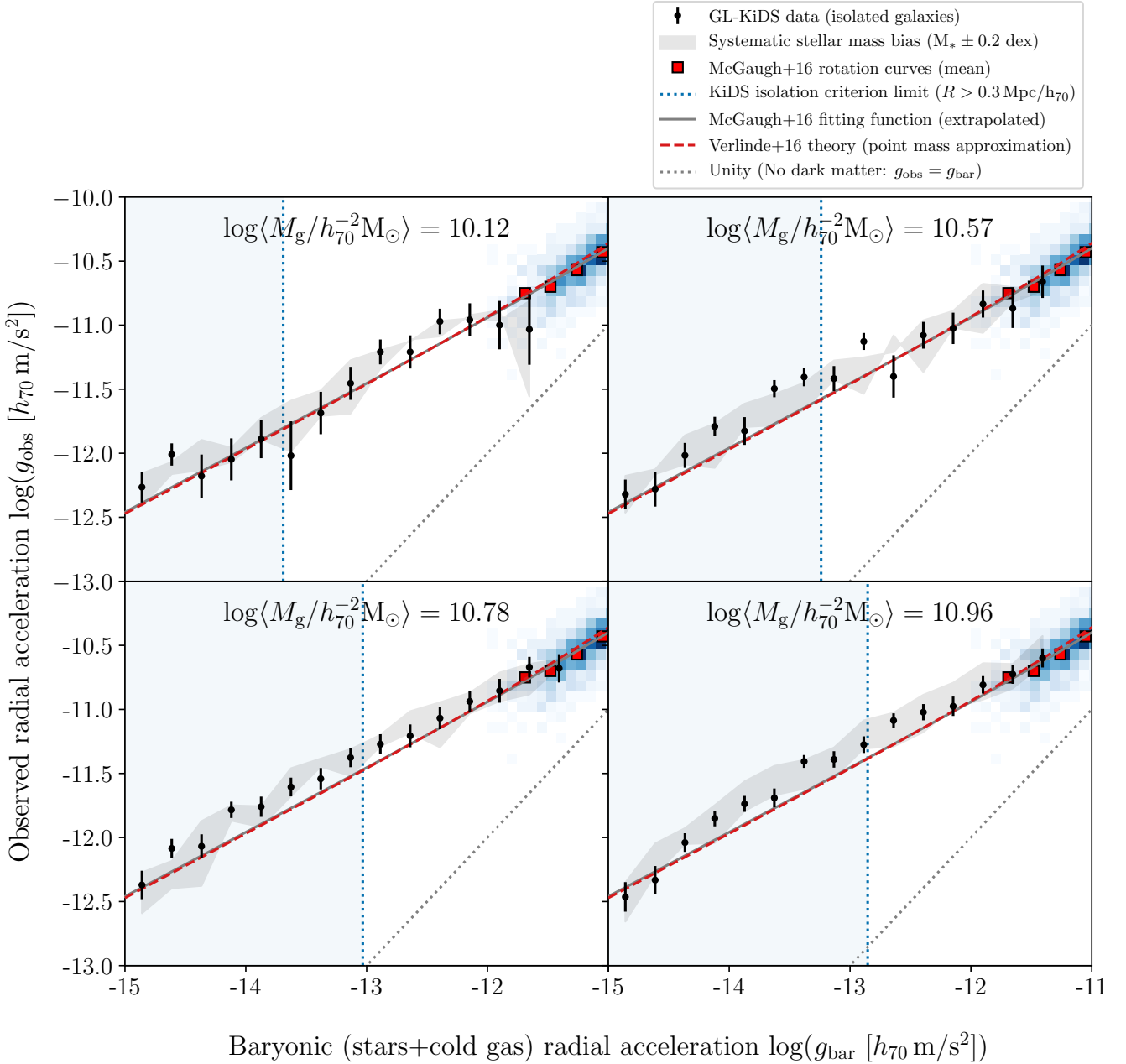


Figure 7. The RAR measured for GL-KiDS lenses (black points with $1 - \sigma$ error bars) divided into four stellar mass bins, with the mean stellar mass of the lenses shown at the top of each panel. At increasing stellar mass, the measurements seem to rise above the predictions from MOND (grey line) and EG (red dashed line). However, at scales larger than $R > 0.3 h^{-1} \text{Mpc}$ (blue dotted line) this could be caused by undetected satellites.

vide our lens sample into four samples based on their stellar mass M_* . We select our M_* -bins to obtain a similar S/N of the lensing signal in each bin, resulting in the following limits: $\log_{10}(M_*/h^{-2} \text{M}_\odot) = [8.5, 10.3, 10.6, 10.8, 11.]$. Figure 7 shows the measured lensing RAR in each bin, with the mean stellar mass of the lenses, $\log_{10}\langle M_*/h^{-2} \text{M}_\odot \rangle = [10.12, 10.57, 10.78, 10.96]$, shown at the top of each panel. Although we still show the M16 RAR measurements from galaxy rotation curves for reference, we zoom in on the lower accelerations that are the focus of this work. At first glance,

there appears to be an upward trend in the RAR of galaxies with larger M_* , which moves the data away from the MOND and EG predictions. Indeed, quantifying the difference between the extended M16 fitting function and our measurement (noting that the prediction for EG is very similar) at *all* scales would result in: $\chi^2_{\text{red}} = 127.90/60 = 2.13$, which would exclude both models at a $\sim 5\sigma$ level. However, at accelerations g_{bar} that correspond to scales larger than $R > 0.3 h^{-1} \text{Mpc}$ (indicated with the blue dotted line) an increasing signal is to be expected, since at these distances

satellite galaxies missed by our isolation criterion might affect the measurement. Galaxies with higher stellar masses reside in denser neighbourhoods, and therefore tend to have more satellites (Baldry et al. 2006; Bolzonella et al. 2010; Brouwer et al. 2016, see e.g.). We therefore calculate the reduced χ^2 values using only the data within $R < 0.3 h^{-1}\text{Mpc}$. In this case the number of free parameters $N = 29$ and $\chi^2_{\text{red}} = 48.94/29 = 1.69$, corresponding to a standard deviation of 2.52σ . The remaining difference could again be alleviated by the possible stellar mass bias ($\Delta M_* = 0.2 \text{ dex}$) which, if it shifts our results downward, would result in: $\chi^2_{\text{red}} = 1.10$, a near perfect fit. If shifted upwards, however, that would result in $\chi^2_{\text{red}} = 4.91$ (8.29σ). This again highlights the grave importance of accurate baryonic mass measurements in determining the RAR, in addition to deep lensing surveys that can detect satellites down to very faint magnitudes (such as the future Euclid survey; Laureijs et al. 2011).

6.1.3 The N17 analytical model

The final analytical prediction we test is the ΛCDM -based model created by N17. In Fig. 8 we show the RAR predicted by this model for a galaxy with a baryonic mass equal to the average stellar + cold gas mass of the lens sample ($\langle \log_{10}(M_{\text{gal}}) \rangle = 10.89$). We compare this prediction to the same observations as shown in Fig. 6. At high accelerations there is a good match between the model and the M16 RAR measurements from galaxy rotation curves, which is expected since the model is designed and confirmed to reproduce these results in the N17 paper. However, at the lower accelerations unique to our lensing measurements the predicted g_{obs} bends down, resulting from the r^{-3} radial dependence of the NFW profile at large scales. While GAMA due to its large error bars could still accommodate the analytical prediction ($\chi^2_{\text{red}} = 15.48/15 = 1.03$), the GL-KiDS results would exclude them with very high confidence ($\chi^2_{\text{red}} = 207.61/8 = 25.95$) even with all data-points beyond the KiDS isolation limit ($R > 3 h^{-1}\text{Mpc}$) removed. However, one could say this was to be expected, since the N17 model is only designed for isolated galaxies. Although we try to select only galaxies which are isolated within the range of our lensing measurement (see Sect. 3.2), it is not guaranteed that we can exclude all possible effects from surrounding total matter. In addition, an underestimation of the amount of baryonic matter around the galaxies can result in a downward slope, as shown in Fig. 4.

From this exercise it is clear that the simple analytical N17 model, while succeeding to describe the RAR at small scales, is not sufficient to reproduce the results at the larger scales ($R > 100 h^{-1}\text{kpc}$) probed by weak lensing. This requires more elaborate modelling within the ΛCDM paradigm, represented by large cosmological simulations such as BAHAMAS and MICE. We will explore the predictions of these simulations in the next section (Sect. 6.2).

6.2 Comparison to ΛCDM simulations

In order to obtain the prediction from ΛCDM simulations, we apply the same isolation criterion to mock lens samples from the MICE and BAHAMAS simulations (see Sect. 2.4

and 2.5). In Fig. 9, BAHAMAS (orange band) is shown as the median result of all galaxies, with the upper and lower limit of the band representing the 16th and 84th percentile. For MICE (red band) we show the result for isolated lenses selected using the true redshifts (lower limit) and using redshifts with a normally distributed random offset of $\sigma_z/(1+z) = 0.018$ (upper limit), in order to emulate the effect of the redshift uncertainty in KiDS (see Sect. 3.2). The measurements are the same GL-KiDS lensing and M16 rotation curve results as shown in Fig. 6, this time compared to the predictions from the two simulations. At the higher accelerations ($g_{\text{bar}} > 10^{-12}$), BAHAMAS appears to overestimate the g_{obs} compared to the M16 and small-scale lensing results. This could be another instance of the general mass mismatch found between predictions based on abundance matching and weak lensing observations, noted by e.g. Leauthaud et al. (2017) and Svensmark et al. (2019). These works showed that their weak lensing observations were too low compared to the predictions of simulations, respectively the BOSS CMASS mock catalogue and the Illustris simulation suite. At lower accelerations ($g_{\text{bar}} < 10^{-12}$), the opposite trend occurs. It is likely that this underestimation of the data by BAHAMAS at larger scales has the same reason as that of the N17 analytic model: in the absence of satellites, the NFW profile goes down as r^{-3} beyond the scale radius. The fact that the data do not show this behaviour either means that the DM haloes of isolated galaxies are not NFW, or that the selected galaxies are not sufficiently isolated. However, our tests both with the KiDS data and the MICE simulations (shown in Fig. 2 and 3 respectively) do not foreshadow an effect of this magnitude. Moreover, Velliscig et al. (2017) likewise noted that the EAGLE simulation underestimates their lensing signal at scales between $0.5 < R < 2 h^{-1}\text{Mpc}$. On the whole it is clear that, at both ends of the acceleration spectrum, BAHAMAS fails to describe our data. Interestingly, the MICE simulation does an excellent job at predicting our measurements, although the resolution of the MICE lensing maps restricts accurate predictions to scales $R > 0.22 h^{-1}\text{Mpc}$. This almost exactly corresponds to the scales where satellites missed by the isolation criterion might impact the lensing signal ($R > 0.3 h^{-1}\text{Mpc}$, dotted blue line). However, the limited width of red band shows that the effect of the KiDS redshift uncertainty on the isolation criterion is relatively small ($\sim 30\%$). Although the predictions from the isolated MICE lenses selected using their true and ‘offset’ redshifts are very alike, strangely the former perform slightly better, resulting in a reduced χ^2 value of $\chi^2_{\text{red}} = 8.60/8 = 1.07$ (0.88σ).

We again split our GL-KiDS lens sample in the same 4 stellar mass bins as in Sect. 6.1, in order to see whether the MICE predictions hold. In Fig. 10 we first show our GL-KiDS lensing measurements and MICE predictions for all lens galaxies, without applying the isolation criterion. This is mainly meant to show the effect of selecting isolated galaxies on the RAR, which is quite striking. Again the MICE simulation is able to predict our measurements: $\chi^2_{\text{red}} = 58.74/32 = 1.84$ (3.00σ), which shows that the clustering simulated within MICE is indeed quite accurate. But the main result is shown in 11, which shows the lensing measurements and MICE predictions for isolated galaxies split in 4 stellar mass bins. In every bin, the MICE simulation does a good job at predicting our measurements. This

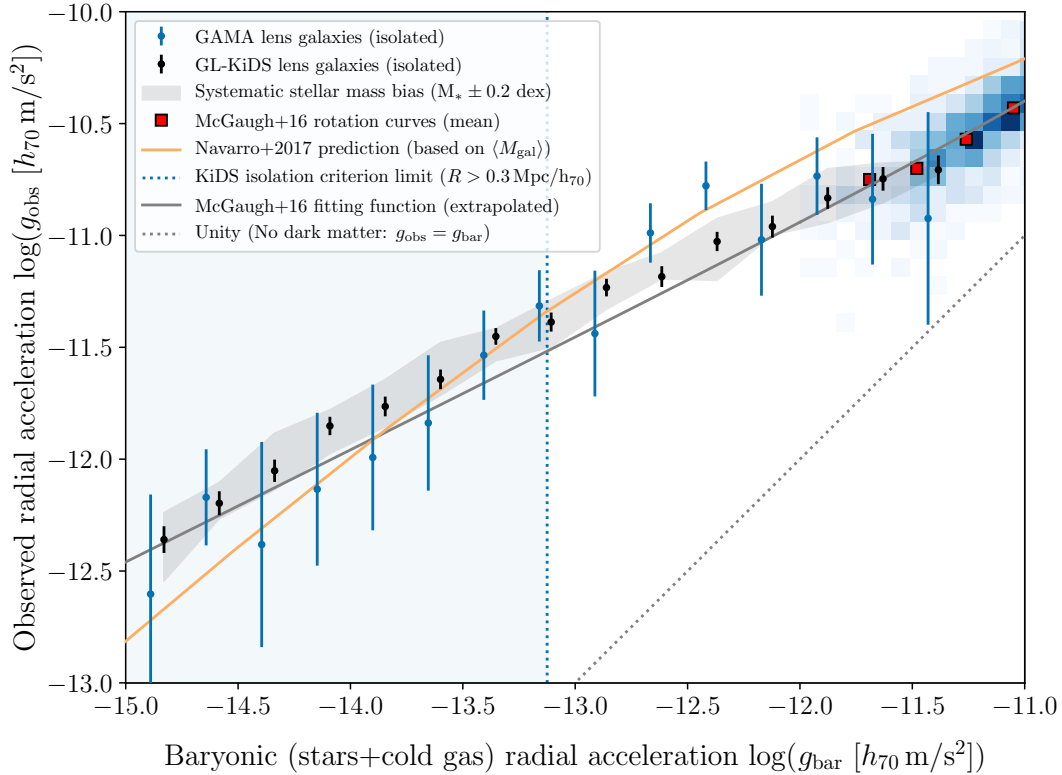


Figure 8. The RAR measured using weak lensing, using the spectroscopic GAMA (blue dots with error bars) and the photometric GL-KiDS (black dots with error bars) isolated lens samples. We compare our results to the analytical Λ CDM-based model created by N17. At higher accelerations there is a good match between the N17 model and the M16 observations, as expected. However, at lower accelerations the model bends down with respect to the lensing measurements.

time, as would be expected, the ‘offset’ MICE results perform slightly better, resulting in an overall reduced χ^2 value of $\chi^2_{\text{red}} = 62.05/32 = 1.94$ (3.26σ).

6.3 Comparison between ellipticals and spirals

As mentioned in Sect. 6.1, both alternative gravity models (MOND and EG) predict approximately the same fixed RAR at $g_{\text{bar}} < 10^{-11}$. The large size of the GL-KiDS lens sample gives us the opportunity to test whether the RAR remains indeed fixed, by dividing our lens galaxies into different samples based on their properties. One property that heavily correlates with galaxy formation history is morphological type, which can be roughly divided into ‘elliptical’ and ‘spiral’. In the Λ CDM framework it is expected that the galaxy-to-halo-mass relation, and therefore the RAR, changes with galaxy type through galaxy formation history (Matthee et al. 2017; Posti et al. 2019; Marasco et al. 2020). For these reasons, it is interesting to compare the RAR of elliptical and spiral galaxies.

The division of galaxies into morphological type can be done based on different parameters, two important ones being Sersic index and color. In order to make sure our results are robust, we measure the RAR for both these splits. The Sersic indices n and $ugri$ magnitudes of all KiDS galaxies with $S/N > 50$ (following Roy et al. (2018)) are measured using the 2DPHOT multi-purpose environment for 2D wide-field image analysis (La Barbera et al. 2008). In Fig. 12 a

2D histogram of $u-r$ galaxy color versus stellar mass shows our two selections: the split based on Sersic index defines ellipticals as galaxies with $n > 2$ (dark blue) and spirals as $n < 2$ (light blue), whereas the split based on $u-r$ color defines ellipticals as galaxies with $m_u - m_r > 2.5$ mag and spirals as $m_u - m_r < 2.5$ mag (above and below the dashed horizontal line, respectively).

In order to isolate the effect of galaxy type from that of stellar mass, we aim to select ellipticals and spirals with the same stellar mass distribution. In Fig. 13 we show the M_* histogram of the two types. From both samples, we remove galaxies until only the overlapping section of both mass distributions remains. In the ideal case this should give us two samples (ellipticals and spirals) with equal stellar mass distributions, both given by the green line. However, since the GL-KiDS M_* measurements contain a $\sigma = 0.21$ dex scatter around the mean, this could cause a systematic shift in the two “equal” M_* distributions resulting from “Eddington bias” (Eddington 1913). We estimate the size of this bias by adding a normally distributed random offset (with $\sigma = 0.21$ dex) to the “true” $\log_{10}(M_*)$ measurements of GL-KiDS, before selecting the two “equal” stellar mass distributions for ellipticals and spirals. We find that the “true” distributions are indeed not equal, but that the mean stellar masses $\langle M_{*,e} \rangle$ and $\langle M_{*,s} \rangle$ of the elliptical and spiral samples differ by 0.057 dex. Of course, this method overlooks that fact that the measured M_* distribution already contains scatter, and is therefore not the “true” M_* distribution. The

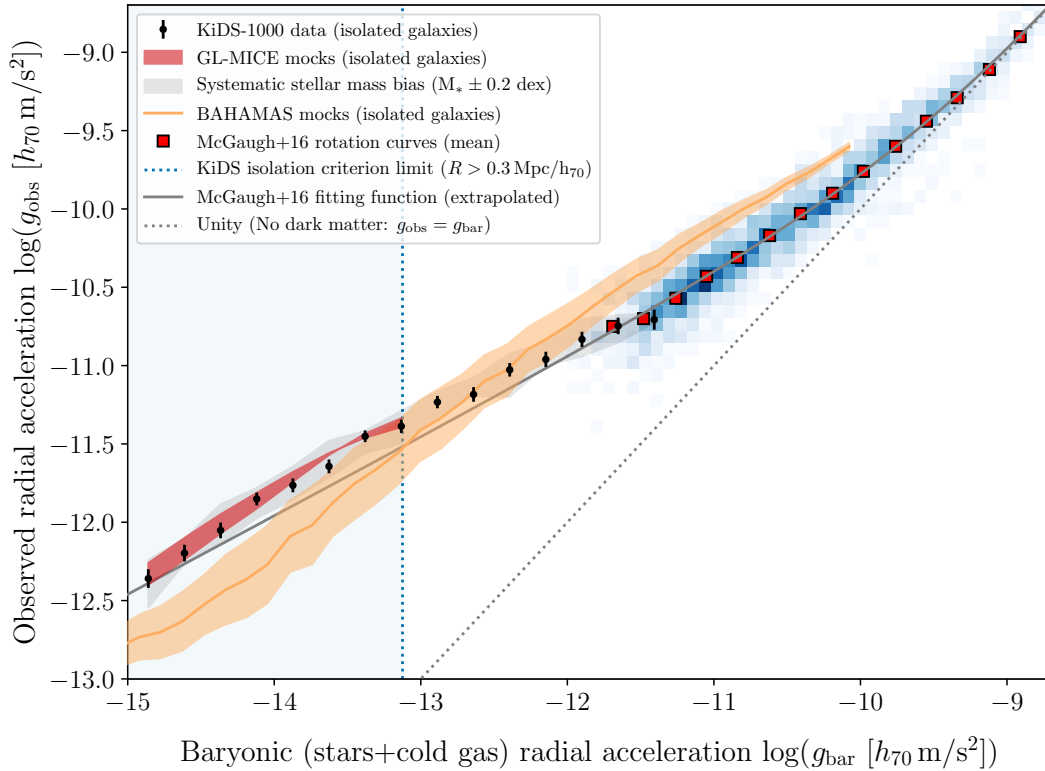


Figure 9. The RAR measured the isolated GL-KiDS lens galaxies (black dots with 1σ error bars) compared to two Λ CDM simulations. The BAHAMAS results (orange band) reflect the median, 16th and 84th percentile of the simulated galaxies, while the MICE results (red band) emulate the effect of the redshift uncertainty in KiDS. BAHAMAS tends to overestimate the M16 rotation curve data at high accelerations, and to underestimate the lensing data at low accelerations. The MICE simulation, though limited to low accelerations by its resolution, succeeds in reproducing the lensing data.

true Eddington effect is likely to be slightly larger, around 0.07 dex.

Figure 14 shows the lensing RAR of GL-KiDS ellipticals and spirals, split by Sérsic index (left panel) and $u - r$ colour (right panel). For this result, we focus on establishing whether there exists a significant difference between the RAR of ellipticals and spirals. Contrary to previous plots, the effect of a 0.2 dex systematic bias in M_* (normally shown by a grey band) is omitted, because this affects both measurements in exactly the same way such that their relative difference does not change. To first order, we can also assume the uncertainty in the KiDS photo- z 's to affect the isolated galaxy selection of both galaxy types in the same way, allowing us to include the full acceleration range into our comparison.

We indeed observe a significant difference between the RAR measurements of the two galaxy types, in agreement with the latest lensing results from Taylor et al. (2020). To quantify this difference, we measure both the reduced χ^2 and the mean offset between the RAR measurements. The χ^2_{red} equals $81.09/15 = 5.41$ (corresponding to 6.59σ) for the lenses split by Sérsic index, and $172.23/15 = 11.48$ for those split by $u - r$ colour. The mean difference between the two RAR measurements is 0.18 dex and 0.29 dex respectively.

However, these conclusions assume that the stellar mass estimates of the two populations are unbiased. To that end we estimate the systematic stellar mass bias be-

tween ellipticals and spirals, $\delta \log_{10}(M_*^{e/s}) = \log_{10}(\langle M_* \rangle_e) - \log_{10}(\langle M_* \rangle_s)$, required to resolve the difference between our two RAR measurements. When trying to estimate the effect of this bias on the RAR, we have to take into account that $\delta M_*^{e/s}$ affects both the estimated acceleration from baryonic mass g_{bar} and the observed acceleration g_{obs} . A bias in M_* would directly determine the baryonic acceleration: $\log_{10}(\delta M_*^{e/s}) = \log(g_{\text{bar}}^{e/s})$. Throughout this work, the observed relation between g_{bar} and g_{obs} at the scales measured by lensing has been approximately $g_{\text{obs}} = \sqrt{g_{\text{bar}}}$. This means that we can roughly estimate the effect on g_{obs} as: $\log_{10}(\delta g_{\text{obs}}^{e/s}) = \log_{10}(\delta M_*^{e/s}) / 2$. Since our measured difference in g_{obs} is at least ~ 0.2 dex, this means $\log_{10}(\delta M_*^{e/s})$ should be at least: $2 \times \log_{10}(\delta g_{\text{obs}}^{e/s}) \sim 0.4$ dex. That is, our observed difference could be resolved should elliptical stellar masses be systematically overestimated, compared to the spiral stellar masses, by 0.4 dex (due to, e.g., Eddington bias, systematic variation of the initial mass function, stellar population synthesis model inaccuracies, etc.). As described above, we have estimated the effect of Eddington bias to be at most 0.07 dex in stellar mass. It is thus very unlikely that the difference we observe is caused by Eddington bias.

6.4 Avoiding g_{bar} : lensing rotation curves

We could add one subsection about lensing rotation curves, see Fig. 15. Henk Hoekstra said he has been planning this

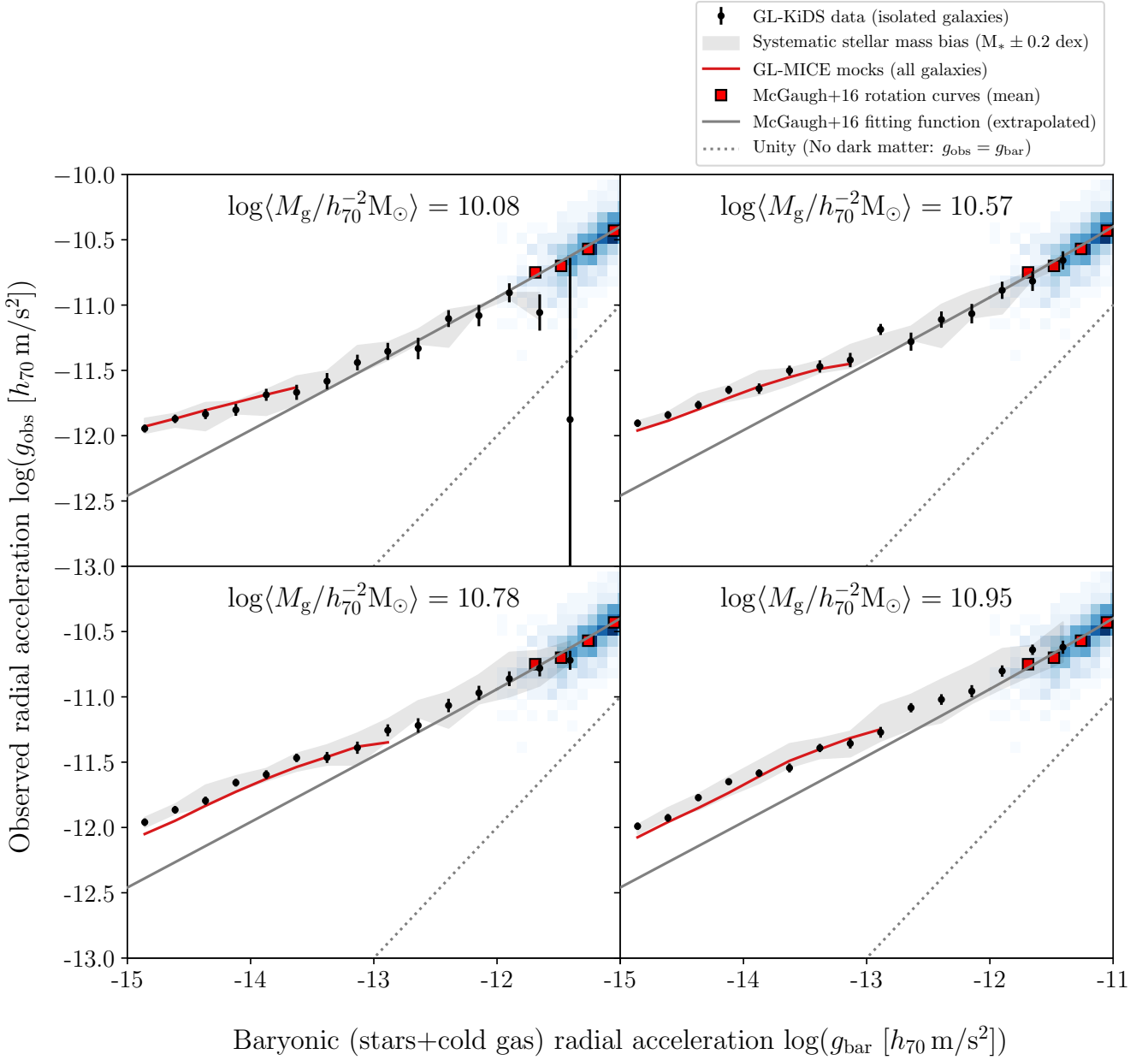


Figure 10. To be written.



for years. Was enthusiastic about how well the lensing fits to the rotation curve data.

7 DISCUSSION AND CONCLUSION

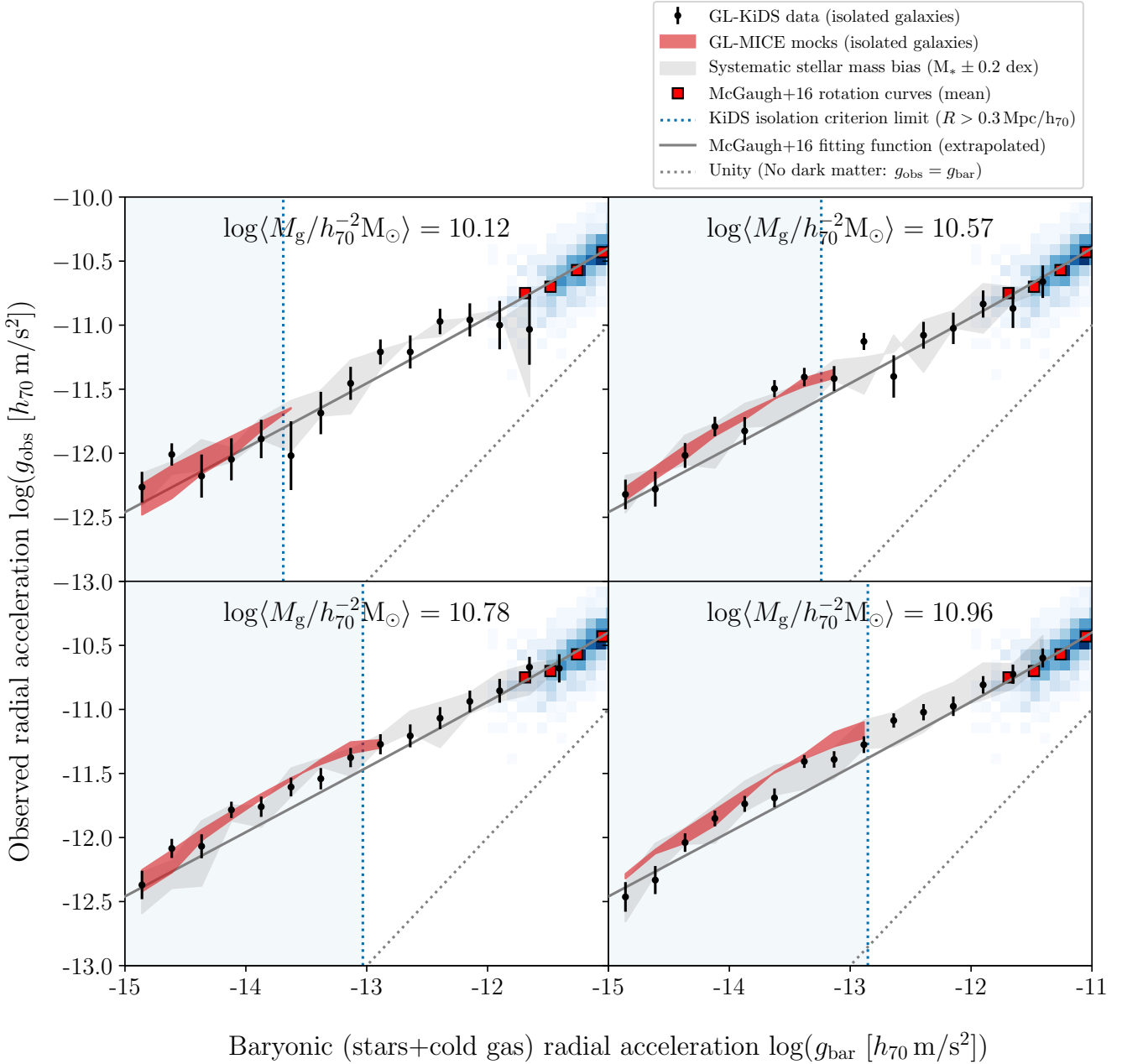
To be written.

ACKNOWLEDGEMENTS

To be written.

REFERENCES

- Abazajian K. N., et al., 2009, [ApJS](#), **182**, 543
 Arnouts S., Cristiani S., Moscardini L., Matarrese S., Lucchin F., Fontana A., Giallongo E., 1999, [MNRAS](#), **310**, 540
 Baldry I. K., Balogh M. L., Bower R. G., Glazebrook K., Nichol R. C., Bamford S. P., Budavari T., 2006, [MNRAS](#), **373**, 469
 Bartelmann M., Schneider P., 2001, [Phys. Rep.](#), **340**, 291
 Begeman K. G., Broeils A. H., Sanders R. H., 1991, [MNRAS](#), **249**, 523
 Behroozi P. S., Marchesini D., Wechsler R. H., Muzzin A., Papovich C., Stefanon M., 2013, [ApJ](#), **777**, L10
 Bell E. F., de Jong R. S., 2001, [ApJ](#), **550**, 212
 Benítez N., 2000, [ApJ](#), **536**, 571
 Bernstein G. M., Guhathakurta P., Raychaudhury S., Giovanelli R., Haynes M. P., Herter T., Vogt N. P., 1994, [AJ](#), **107**, 1962

Figure 11. *To be written.*

Bertin E., Arnouts S., 1996, *A&AS*, **117**, 393
 Bertone G., Tait T. M. P., 2018, *Nature*, **562**, 51
 Bertone G., Hooper D., Silk J., 2005, *Phys. Rep.*, **405**, 279
 Bilicki M., et al., 2017, preprint, ([arXiv:1709.04205](https://arxiv.org/abs/1709.04205))
 Blake C., et al., 2011, *MNRAS*, **415**, 2892
 Bolzonella M., et al., 2010, *A&A*, **524**, A76
 Boselli A., et al., 2010, *PASP*, **122**, 261
 Boselli A., Cortese L., Boquien M., Boissier S., Catinella B., Lagos C., Saintonge A., 2014, *A&A*, **564**, A66
 Bosma A., 1981, *AJ*, **86**, 1791
 Brouwer M. M., et al., 2016, *MNRAS*, **462**, 4451
 Brouwer M. M., et al., 2017, *MNRAS*, **466**, 2547
 Brouwer M. M., et al., 2018, *MNRAS*, **481**, 5189
 Bruzual G., Charlot S., 2003, *MNRAS*, **344**, 1000

Capaccioli M., Schipani P., 2011, *The Messenger*, **146**, 2
 Carretero J., Castander F. J., Gaztañaga E., Crocce M., Fosalba P., 2015, *MNRAS*, **447**, 646
 Chabrier G., 2003, *PASP*, **115**, 763
 Crocce M., Castander F. J., Gaztañaga E., Fosalba P., Carretero J., 2015, *MNRAS*, **453**, 1513
 Crocker A. F., Bureau M., Young L. M., Combes F., 2011, *MNRAS*, **410**, 1197
 Davis M., Efstathiou G., Frenk C. S., White S. D. M., 1985, *ApJ*, **292**, 371
 Davis T. A., et al., 2013, *MNRAS*, **429**, 534
 Desmond H., 2017, *MNRAS*, **464**, 4160
 Dolag K., Borgani S., Murante G., Springel V., 2009, *MNRAS*, **399**, 497

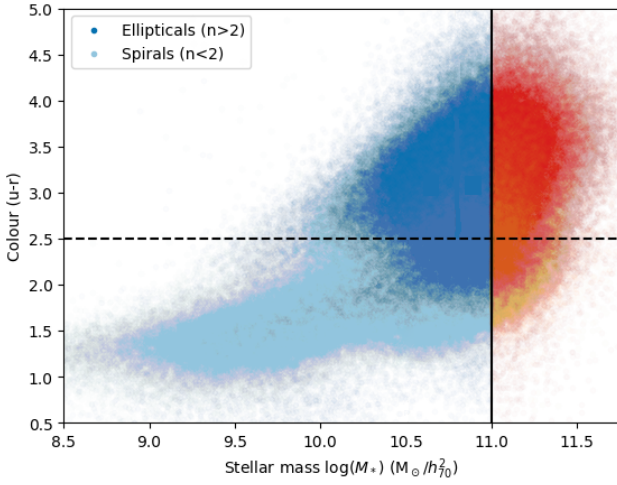


Figure 12. To be written.

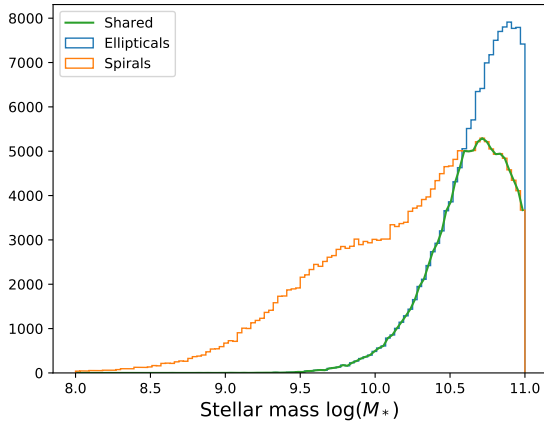
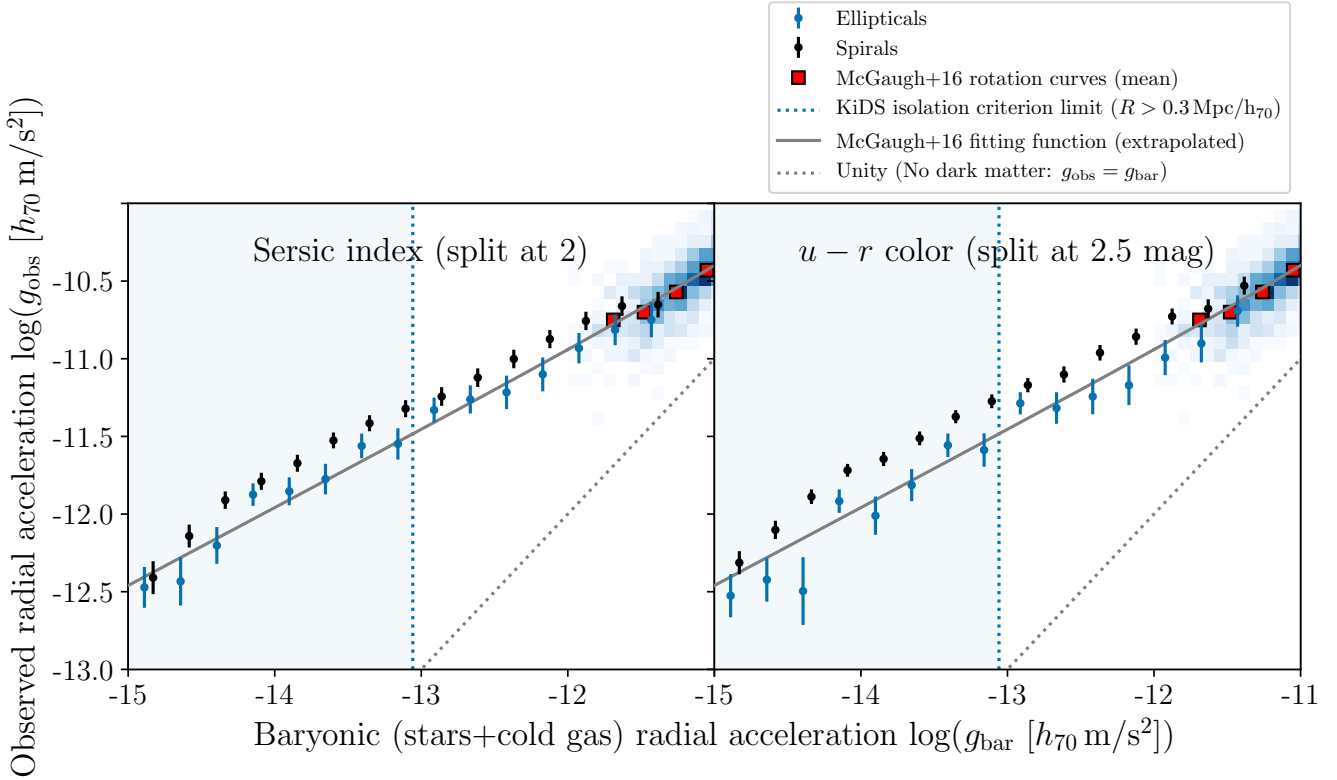


Figure 13. To be written.

Driver S. P., et al., 2011, *MNRAS*, **413**, 971
 Dvornik A., et al., 2017, *MNRAS*, **468**, 3251
 Dvornik A., et al., 2018, preprint, ([arXiv:1802.00734](https://arxiv.org/abs/1802.00734))
 Eddington A. S., 1913, *MNRAS*, **73**, 359
 Edge A., Sutherland W., Kuijken K., Driver S., McMahon R., Eales S., Emerson J. P., 2013, *The Messenger*, **154**, 32
 Eisenstein D. J., et al., 2005, *ApJ*, **633**, 560
 Erben T., et al., 2013, *MNRAS*, **433**, 2545
 Faulkner T., Guica M., Hartman T., Myers R. C., Van Raamsdonk M., 2014, *Journal of High Energy Physics*, **3**, 51
 Fenech Conti I., Herbonnet R., Hoekstra H., Merten J., Miller L., Viola M., 2017, *MNRAS*, **467**, 1627
 Fischer P., et al., 2000, *AJ*, **120**, 1198
 Foreman-Mackey D., Hogg D. W., Lang D., Goodman J., 2013, *PASP*, **125**, 306
 Fosalba P., Gaztañaga E., Castander F. J., Manera M., 2008, *MNRAS*, **391**, 435
 Fosalba P., Gaztañaga E., Castander F. J., Crocce M., 2015a, *MNRAS*, **447**, 1319
 Fosalba P., Crocce M., Gaztañaga E., Castander F. J., 2015b, *MNRAS*, **448**, 2987
 Fukugita M., Peebles P. J. E., 2004, *ApJ*, **616**, 643

Fukugita M., Hogan C. J., Peebles P. J. E., 1998, *ApJ*, **503**, 518
 Hildebrandt H., et al., 2012, *MNRAS*, **421**, 2355
 Hildebrandt H., et al., 2017, *MNRAS*, **465**, 1454
 Hinshaw G., et al., 2013, *The Astrophysical Journal Supplement Series*, **208**, 19
 Hoekstra H., Yee H. K. C., Gladders M. D., 2004, *ApJ*, **606**, 67
 Hoffmann K., Bel J., Gaztañaga E., Crocce M., Fosalba P., Castander F. J., 2015, *MNRAS*, **447**, 1724
 Ilbert O., et al., 2006, *A&A*, **457**, 841
 Ilbert O., et al., 2009, *ApJ*, **690**, 1236
 Jacobson T., 1995, *Physical Review Letters*, **75**, 1260
 Jacobson T., 2016, *Physical Review Letters*, **116**, 201101
 de Jong J. T. A., Verdoes Kleijn G. A., Kuijken K. H., Valentijn E. A., 2013, *Experimental Astronomy*, **35**, 25
 de Jong J. T. A., et al., 2017, *A&A*, **604**, A134
 Keller B. W., Wadsley J. W., 2017, *ApJ*, **835**, L17
 Kirkman D., Tytler D., Suzuki N., O'Meara J. M., Lubin D., 2003, *ApJS*, **149**, 1
 Kuijken K., 2008, *A&A*, **482**, 1053
 Kuijken K., 2011, *The Messenger*, **146**, 8
 Kuijken K., et al., 2015, *MNRAS*, **454**, 3500
 Kuijken K., et al., 2019, arXiv e-prints, p. [arXiv:1902.11265](https://arxiv.org/abs/1902.11265)
 La Barbera F., de Carvalho R. R., Kohl-Moreira J. L., Gal R. R., Soares-Santos M., Capaccioli M., Santos R., Sant'Anna N., 2008, *PASP*, **120**, 681
 Laureijs R., et al., 2011, preprint, ([arXiv:1110.3193](https://arxiv.org/abs/1110.3193))
 Leauthaud A., et al., 2017, *MNRAS*, **467**, 3024
 Lelli F., McGaugh S. S., Schombert J. M., 2016, *AJ*, **152**, 157
 Lelli F., McGaugh S. S., Schombert J. M., 2017, *MNRAS*, **468**, L68
 von der Linden A., et al., 2014, *MNRAS*, **439**, 2
 Liske J., et al., 2015, *MNRAS*, **452**, 2087
 Ludlow A. D., Navarro J. F., Angulo R. E., Boylan-Kolchin M., Springel V., Frenk C., White S. D. M., 2014, *MNRAS*, **441**, 378
 Ludlow A. D., et al., 2017, *Phys. Rev. Lett.*, **118**, 161103
 Mandelbaum R., 2015, in Cappellari M., Courteau S., eds, *IAU Symposium Vol. 311, Galaxy Masses as Constraints of Formation Models*. pp 86–95 ([arXiv:1410.0734](https://arxiv.org/abs/1410.0734))
 Mandelbaum R., Seljak U., Kauffmann G., Hirata C. M., Brinkmann J., 2006, *MNRAS*, **368**, 715
 Marasco A., Posti L., Oman K., Famaey B., Cresci G., Fraternali F., 2020, arXiv e-prints, p. [arXiv:2005.01724](https://arxiv.org/abs/2005.01724)
 Matthee J., Schaye J., Crain R. A., Schaller M., Bower R., Theuns T., 2017, *MNRAS*, **465**, 2381
 McCarthy I. G., Schaye J., Bird S., Le Brun A. M. C., 2017, *MNRAS*, **465**, 2936
 McCarthy I. G., Bird S., Schaye J., Harnois-Deraps J., Font A. S., van Waerbeke L., 2018, *MNRAS*, **476**, 2999
 McFarland J. P., Verdoes-Kleijn G., Sikkema G., Helmich E. M., Boxhoorn D. R., Valentijn E. A., 2013, *Experimental Astronomy*, **35**, 45
 McGaugh S. S., 2004, *ApJ*, **609**, 652
 McGaugh S. S., 2012, *AJ*, **143**, 40
 McGaugh S. S., Schombert J. M., Bothun G. D., de Blok W. J. G., 2000, *ApJ*, **533**, L99
 McGaugh S. S., Lelli F., Schombert J. M., 2016, *Physical Review Letters*, **117**, 201101
 Mentuch Cooper E., et al., 2012, *ApJ*, **755**, 165
 Milgrom M., 1983, *ApJ*, **270**, 365
 Milgrom M., Sanders R. H., 2008, *ApJ*, **678**, 131
 Miller L., Kitching T. D., Heymans C., Heavens A. F., van Waerbeke L., 2007, *MNRAS*, **382**, 315
 Miller L., et al., 2013, *MNRAS*, **429**, 2858
 Navarro J. F., Benítez-Llambay A., Fattahi A., Frenk C. S., Ludlow A. D., Oman K. A., Schaller M., Theuns T., 2017, *MNRAS*, **471**, 1841
 Nicastrò F., et al., 2018, *Nature*, **558**, 406

Figure 14. *To be written.*

Padmanabhan T., 2010, *Reports on Progress in Physics*, **73**, 046901
Pierce M. J., Tully R. B., 1988, *ApJ*, **330**, 579
Planck VI x., 2018, arXiv e-prints, p. arXiv:1807.06209
Planck XVI x., 2014, *A&A*, **571**, A16
Pohlen M., et al., 2010, *A&A*, **518**, L72
Posti L., Fraternali F., Marasco A., 2019, *A&A*, **626**, A56
Robotham A. S., et al., 2011, *MNRAS*, **416**, 2640
Roy N., et al., 2018, *MNRAS*, **480**, 1057
Rubin V. C., 1983, *Scientific American*, **248**, 96
Sadeh I., Abdalla F. B., Lahav O., 2016, *PASP*, **128**, 104502
Sanders R. H., 1986, *MNRAS*, **223**, 539
Sanders R. H., 1996, *ApJ*, **473**, 117
Sanders R. H., Noordermeer E., 2007, *MNRAS*, **379**, 702
Schneider P., Kochanek C. S., Wambsganss J., 2006, *Gravitational Lensing: Strong, Weak and Micro*. Saas-Fee Advanced Courses, Swiss Society for Astrophysics and Astronomy, Springer, Berlin, Heidelberg, <http://cds.cern.ch/record/1339023>
Shull J. M., Smith B. D., Danforth C. W., 2012, *ApJ*, **759**, 23
Sifón C., et al., 2015, *MNRAS*, **454**, 3938
Spergel D. N., et al., 2003, *ApJS*, **148**, 175
Springel V., White S. D. M., Tormen G., Kauffmann G., 2001, *MNRAS*, **328**, 726
Svensmark J., Martizzi D., Agnello A., 2019, arXiv e-prints, p. arXiv:1906.00975
Taylor E. N., et al., 2011, *MNRAS*, **418**, 1587
Taylor E. N., et al., 2020, arXiv e-prints, p. arXiv:2006.10040
Tully R. B., Fisher J. R., 1977, *A&A*, **54**, 661
Tumlinson J., Peebles M. S., Werk J. K., 2017, *ARA&A*, **55**, 389
van Uitert E., et al., 2016, *MNRAS*, **459**, 3251
Velliscig M., et al., 2017, *MNRAS*, **471**, 2856
Verlinde E., 2011, *Journal of High Energy Physics*, **4**, 29

Verlinde E. P., 2016, preprint, (arXiv:1611.02269)
Viel M., Becker G. D., Bolton J. S., Haehnelt M. G., 2013, *Phys. Rev. D*, **88**, 043502
Viola M., et al., 2015, *MNRAS*, **452**, 3529
Wright A. H., et al., 2017, *MNRAS*, **470**, 283
Wu X., Kroupa P., 2015, *MNRAS*, **446**, 330
Zehavi I., et al., 2011, *ApJ*, **736**, 59
Zwicky F., 1937, *ApJ*, **86**, 217

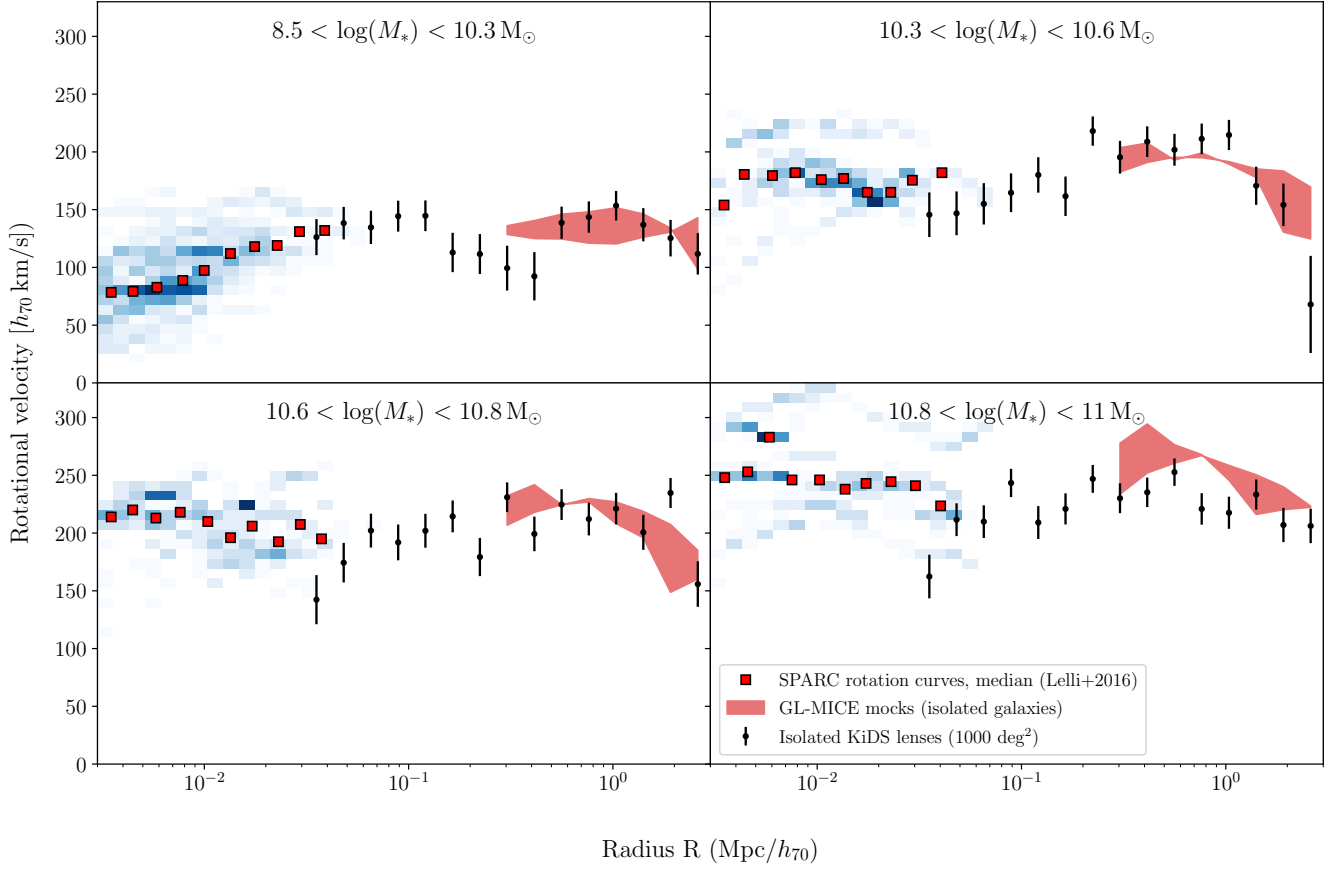


Figure 15. To be written.

APPENDIX A: EXCESS SURFACE DENSITY PROFILE OF A PIECE-WISE POWER LAW VOLUME DENSITY PROFILE

The excess surface density profile is measured in a series of discrete radial bins with edges R_m . The representative value at the centre of the bin – here we define the bin centre as $\frac{1}{2}(R_m + R_{m+1})$, i.e. not the ‘logarithmic centre’ $\sqrt{R_m R_{m+1}}$, which ensures accuracy in the calculation of the mean enclosed surface density – is $\Delta\Sigma_m = \bar{\Sigma}_m - \Sigma_m$, where $\bar{\Sigma}_m$ is the mean surface density within $\frac{1}{2}(R_m + R_{m+1})$ and Σ_m is the surface density averaged over the interval $[R_m, R_{m+1})$. We give an expression for this discrete excess surface density profile in terms of the parametric form for $\rho(r)$ given in Eq. 17.

The mean enclosed surface density is:

[@Kyle: Somehow there appears to be a huge gap between this line and the equation. Some strange Latex bug. How do we solve this?]

$$\bar{\Sigma}_m = \frac{1}{\pi R_m R_{m+1}} \left[I_1(0, \sqrt{R_0 R_1}, \tilde{a}_0, \tilde{b}_0) + \sum_{k=0}^m I_1(\sqrt{R_m R_{m+1}}, \sqrt{R_{m+1} R_{m+2}}, \tilde{a}_m, \tilde{b}_m) \right] \quad (\text{A1})$$

$$\tilde{a}_m = \frac{\log(\Sigma_{m+1}) - \log(\Sigma_m)}{\frac{1}{2}(\log(R_{m+2}) - \log(R_m))} \quad (\text{A2})$$

$$\tilde{b}_m = \log(\Sigma_m) - \frac{1}{2}\tilde{a}_m \log(R_m R_{m+1}) \quad (\text{A3})$$

$$I_1(R_i, R_j, \tilde{a}, \tilde{b}) = \frac{2\pi e^{\tilde{b}}}{\tilde{a} + 2} (R_j^{a+2} - R_i^{a+2}) \quad (\text{A4})$$

and the local surface density is given by:

$$\Sigma_m = \sum_{n=0}^{N-1} \begin{cases} 0 & \text{if } r_{n+1} < R_m \\ \frac{4e^{b_n}}{R_{m+1}^2 - R_m^2} (-I_2(r_{n+1}, R_m, a_n)) & \text{if } r_n < R_m \text{ and } R_m \leq r_{n+1} < R_{m+1} \\ \frac{4e^{b_n}}{R_{m+1}^2 - R_m^2} (I_2(r_{n+1}, R_{m+1}, a_n) - I_2(r_{n+1}, R_m, a_n)) & \text{if } r_n < R_m \text{ and } r_{n+1} \geq R_{m+1} \\ \frac{4e^{b_n}}{R_{m+1}^2 - R_m^2} (I_2(r_{n+1}, r_n, a_n) - I_2(r_{n+1}, R_m, a_n) \\ \quad + I_2(r_n, R_m, a_n) + I_2(r_{n+1}, R_{m+1}, a_n) \\ \quad - I_2(r_{n+1}, r_n, a_n)) & \text{if } R_m \leq r_n < R_{m+1} \text{ and } r_n \geq R_{m+1} \\ \frac{4e^{b_n}}{R_{m+1}^2 - R_m^2} (I_2(r_{n+1}, R_{m+1}, a_n) - I_2(r_{n+1}, R_m, a_n) \\ \quad - I_2(r_n, R_{m+1}, a_n) + I_2(r_n, R_m, a_n)) & \text{if } r_n \geq R_{m+1} \\ \frac{4e^{b_n}}{R_{m+1}^2 - R_m^2} (I_2(r_{n+1}, r_n, a_n) - I_2(r_{n+1}, R_m, a_n) \\ \quad + I_2(r_n, R_m, a_n) - I_2(r_{n+1}, r_n, a_n)) & \text{if } r_n \geq R_m \text{ and } r_{n+1} < R_m \end{cases} \quad (\text{A5})$$

$$I_2(r, R, a) = \begin{cases} -\frac{1}{3} R^{a+3} \left(\frac{r^2}{R^2} - 1 \right)^{\frac{3}{2}} {}_2F_1 \left(\frac{3}{2}, -\frac{a}{2}; \frac{5}{2}; 1 - \frac{r^2}{R^2} \right) & \text{if } r \text{ is finite} \\ \frac{\sqrt{\pi}}{2} \frac{\Gamma(-\frac{a+1}{2})}{\Gamma(-\frac{a}{2})} \frac{R^{a+3}}{a+3} & \text{if } r = \infty \end{cases} \quad (\text{A6})$$

where ${}_2F_1(\cdot, \cdot; \cdot; \cdot)$ is the Gaussian hypergeometric function and $\Gamma(\cdot)$ is the Gamma function. We assume that the power law slope in the innermost bin continues to $r = 0$, and that that in the outermost bin continues to $r \rightarrow \infty$. When inverting $\Delta\Sigma(\rho)$, we impose uninformative priors on the power law slopes except those constraints required to guarantee that the total mass is finite and the calculation is numerically stable.

This paper has been typeset from a \LaTeX file prepared by the author.